



Controls on the formation of stratabound dolostone bodies, Hammam Faraun Fault block, Gulf of Suez

DOI:

[10.1111/sed.12454](https://doi.org/10.1111/sed.12454)

Document Version

Accepted author manuscript

[Link to publication record in Manchester Research Explorer](#)

Citation for published version (APA):

Hirani, J., Bastesen, E., Boyce, A., Corlett, H., Gawthorpe, R. L., Hollis, C., John, C. M., Robertson, H., Rotevatn, A., & Whitaker, F. (2018). Controls on the formation of stratabound dolostone bodies, Hammam Faraun Fault block, Gulf of Suez. *Sedimentology*, 65(6), 1973-2002. <https://doi.org/10.1111/sed.12454>

Published in:

Sedimentology

Citing this paper

Please note that where the full-text provided on Manchester Research Explorer is the Author Accepted Manuscript or Proof version this may differ from the final Published version. If citing, it is advised that you check and use the publisher's definitive version.

General rights

Copyright and moral rights for the publications made accessible in the Research Explorer are retained by the authors and/or other copyright owners and it is a condition of accessing publications that users recognise and abide by the legal requirements associated with these rights.

Takedown policy

If you believe that this document breaches copyright please refer to the University of Manchester's Takedown Procedures [<http://man.ac.uk/04Y6Bo>] or contact uml.scholarlycommunications@manchester.ac.uk providing relevant details, so we can investigate your claim.



Controls on the formation of stratabound dolostone bodies, Hammam Faraun Fault block, Gulf of Suez

Jesal Hirani^{a*}, Eivind Bastesen^b, Adrian Boyce^c, Hilary Corlett^a, Rob Gawthorpe^b, Cathy Hollis^a, Cédric M. John^e, Hamish Robertson^d, Atle Rotevatn^b, and Fiona Whitaker^d

^{a*} *The University of Manchester, School of Earth, Atmospheric and Environmental Sciences, The University of Manchester, Manchester, M13 9PL, UK*

^b *University of Bergen, Department of Geovitenskap, Realfagbygget, Allegaten 41, 5007, Norway*

^c *NERC Isotope Community Support Facility, Scottish Universities Environmental Research Centre, Rankine Avenue, Scottish Enterprise Technology Park, East Kilbride, G75 0QF, UK*

^d *The University of Bristol, School of Earth Sciences, Wills Memorial Building, Queens Road, Bristol, BS8 1RJ, UK*

^e *Department of Earth Science and Engineering, Imperial College London, Prince Consort Road, London SW7 2AZ, UK*

jesal_hirani@hotmail.com

Eivind.Bastesen@uni.no

Adrian.Boyce@glasgow.ac.uk

hilarycdn@gmail.com

rob.gawthorpe@geo.uib.no

cathy.hollis@manchester.ac.uk

cedric.john@imperial.ac.uk

atle.rotevatn@geo.uib.no

Hamish.Robertson@bristol.ac.uk

Fiona.Whitaker@bristol.ac.uk

Abstract

Dolomitization is commonly associated with crustal-scale faults, but tectonic rejuvenation, diagenetic overprinting and a fluid and Mg mass-imbalance often makes it difficult to determine the dolomitization mechanism. This study considers differential dolomitization of the Eocene Thebes Fm. on the Hammam Faraun Fault (HFF) block, Gulf of Suez, which has undergone a simple history of burial and exhumation as a result of rifting. Stratabound dolostone bodies occur selectively within remobilized sediments (debrites and turbidites) in the lower Thebes Formation and extend into the footwall of, and for up to 2 km away from, the HFF. They are offset by the N-S trending Gebel fault, which was active during the earliest phases of rifting, suggesting dolomitization occurred between rift initiation (26 Ma) and rift climax (15 Ma).

Geochemical data suggest that dolomitization occurred from evaporated (~1.43 concentration) seawater at $<80^{\circ}\text{C}$. Geothermal convection is interpreted to have occurred as seawater was drawn down surface-breaching faults into the Nubian sandstone aquifer, convected and discharged into the lower Thebes Formation via the HFF. Assuming an approximate 10 My window for dolomitization, a horizontal velocity of ~0.7 m/yr into the Thebes Fm is calculated, with fluid flux and reactivity likely to have been facilitated by fracturing. Although fluids were at least marginally hydrothermal, stratabound dolostone bodies do not contain saddle dolomite and there is no evidence of hydrobrecciation. This highlights how misleading dolostone textures can be as a proxy for the genesis and spatial distribution of such bodies in the subsurface. Overall, this study provides an excellent example of how fluid flux may occur during the earliest phases of rifting, and the importance of crustal-scale faults on fluid flow from the onset of their growth. Furthermore, we present a mechanism for dolomitization from seawater that has none of the inherent mass balance problems of classical, conceptual models of hydrothermal dolomitization.

Key words:

Rift initiation, stratabound dolostone, dolomitization, geothermal convection

52 Introduction

53 Stratabound dolostone bodies associated with faults are often interpreted to be genetically related to
 54 massive so-called hydrothermal dolomite (HTD) bodies (e.g. Southern Italy (Cervato, 1990; Boni *et al.*,
 55 2000), Northern Spain (Gasparrini *et al.*, 2006; López-Horgue *et al.*, 2010; Dewit *et al.*, 2014),
 56 Lebanon and Iran ((Nader *et al.*, 2007; Sharp *et al.*, 2010) and Western Canada (Davies and Smith,
 57 2006; Lonnee and Machel, 2006)). In these examples, the dolomitizing fluids utilise deep-seated
 58 structural lineaments, usually normal or strike-slip faults, as conduits for the upward flow of fluids
 59 derived from beneath the dolomitized succession. Pervasive dolomitization is interpreted to take place
 60 adjacent to the fault, forming massive, non-stratabound dolostone bodies, whilst stratabound bodies
 61 form as fluids flux along beds away from the fault. This results in a 'Christmas tree' shaped geobody,
 62 sometimes hundreds of metres or more in lateral extent, which may be targeted for hydrocarbon
 63 exploration.

64 There has been some success in the exploration and production of such bodies within the Western
 65 Canadian Sedimentary Basin (e.g. Davies and Smith, 2006) with only a few examples outside this
 66 region (e.g. Panuke Field, Canada; Wierzbicki *et al.*, 2006). Overall, the play has not proven globally
 67 successful because of a lack of either reservoir presence or volume. Nonetheless, HTD still has
 68 enormous economic potential as a host for low temperature Mississippi-Valley type (MVT) deposits
 69 within the USA, Canada and UK (e.g. Gregg, 2004). Nevertheless, the conceptual model for the
 70 formation of HTD has come under scrutiny, since many studies fail to adequately explain the source
 71 and drive mechanism for dolomitizing fluids and source of magnesium.

72 On the Hammam Faraun Fault (HFF) block, Gulf of Suez, non-stratabound dolomitization is observed
 73 in proximity to the HFF, with numerous, discontinuous stratabound dolostone bodies extending into
 74 the footwall for up to 2 km. Hollis *et al.* (2017) demonstrated that in this well-exposed example, the
 75 stratabound dolostone pre-dates, and is not genetically related to, , cross-cutting non-stratabound
 76 dolostone. This is contrary to the interpretation of many dolostone bodies formed in proximity to faults.
 77 This paper provides detailed characterisation of these stratabound dolostone bodies through field
 78 observations and measurements, petrography and geochemistry. It discusses and tests the flow
 79 mechanisms responsible for their formation, calculates the mass balance and presents a conceptual
 80 model for dolomitization in the context of the structural evolution of the fault block. The results provide
 81 an important insight into fluid flux and diagenesis on carbonate platforms in the earliest stages of rift
 82 initiation.

83 Geological setting

84 The Gulf of Suez is a failed intracontinental rift that forms the northern continuation of the Red Sea rift,
 85 which originated during the early Palaeozoic as a narrow embayment of the Tethys Ocean. The rift

was rejuvenated 23 Ma, during the separation of the African Plate from the Arabian Plate in the Late Oligocene (Jarrige *et al.*, 1990; Patton *et al.*, 1994; Sharp *et al.*, 2000; Younes and McClay, 2002; Bosworth *et al.*, 2005). From the Middle Miocene (14–12 Ma), stress in the southern Gulf of Suez transferred to the Aqaba–Levant transform boundary, formed by the collision of Arabia with Eurasia, and dramatically slowed down extension rates in the Gulf of Suez (Montenat *et al.*, 1988; Bosworth *et al.*, 2005).

The Suez rift is bounded by two major sets of marginal faults that strike parallel to the length of the Gulf (Alsharhan and Salah, 1995). The normal faults are linked by shorter, slightly oblique transfer faults, resulting in an *en echelon* fault pattern (Gawthorpe and Hurst, 1993; Patton *et al.*, 1994; Sharp *et al.*, 2000). In cross section, the rift is characterised by large, widely spaced half grabens with eroded crests and deep hanging-wall basins (Moustafa and Abdeen 1992; Knott *et al.*, 1995; Sharp *et al.*, 2000; Khalil and McClay, 2001). Each half graben consists of several fault blocks (Robson, 1971), with the study area located in the Hammam Faraun Fault (HFF) block (Fig. 1). During the Oligo-Miocene, basaltic dykes and sills (dated as 22 and 26 Ma; Montenat *et al.*, 1986; Moustafa and Abdeen 1992; Patton *et al.*, 1994) were emplaced in the study area and provide the first stratigraphic evidence for rifting. Overall, volcanism in the Gulf of Suez is minor, however a large basaltic province has been described in northern Egypt, with a geochemical signature typical of primary magmas extruded over 1–2 Myr at around 23 Ma (Bosworth *et al.*, 2015).

The HFF is a major crustal scale fault, with greater than 4 km of displacement (Jackson *et al.*, 2005), controlling the position of the present day shoreline. The HFF block is the footwall of the HFF and is exposed on the western side of the Sinai Peninsula, bounded to the east and south by the broadly NW-SE trending Thal Fault (Fig. 1). Sediments within the fault block (Fig. 1B) dip north-eastwards, controlled by the orientation of the HFF (Robson, 1971; Moustafa and Abdeen, 1992; Jackson *et al.*, 2005; Leppard and Gawthorpe, 2006). During the earliest stages of rifting, movement was focussed primarily along the Thal Fault and its isolated fault segments, including a N-S fault (referred to as the Gebel Fault; Fig. 2) which intersects the HFF and has a maximum displacement of 300 m. The presence of early syn-rift (Miocene) sediments that unconformably overlie pre-rift carbonates within the hanging wall of this fault date movement to rift initiation (~26 Ma; Woodman, 2009). From 17–15 Ma, displacement focussed and localised onto the HFF, with no further movement along the Thal Fault and its associated segments (Gawthorpe *et al.*, 2003). Since the HFF is located immediately offshore of the study area, the hanging wall is not exposed and has not been imaged by seismic data.

The damage zone of the HFF is exposed in the footwall and comprises fabric-destructive, non-stratabound dolostone (massive bodies) that are pervasively dissected by non-stratabound calcite, dolomite, gypsum and iron oxide cemented fractures (Korneva *et al.*, 2017; Hirani *et al.*, in prep). Hydrobrecciation was not observed, except within a 30 m wide fracture corridor that bounds the massive dolostone body (Hirani *et al.*, in prep). Away from the damage zone, fracture spacing

122 increases with bed thickness, with a higher fracture density (narrower spacing) in dolostone compared
123 to limestone beds (Korneva *et al.*, 2017).

124 The pre-rift stratigraphy of the HFF block comprises a 2000 m thick sedimentary section, which
125 overlies Precambrian igneous and metamorphic basement rocks (Fig. 1) (Moustafa and Abdeen,
126 1992; Moustafa, 1996). The basement is overlain by a thick, undifferentiated package of quartz
127 arenitic sandstones, the Nubian Sandstone, which has very high average porosity and permeability
128 (26%, >1 D; Nabawy *et al.*, 2009) and is an important modern day aquifer. The overlying Mesozoic
129 succession (Sudr, Matulla, Raha, Wata and Esna; Fig. 1B) comprises mixed carbonate and siliciclastic
130 sediments with a moderate porosity but low permeability (7-12%, <0.01 mD; Zalat *et al.*, 2010;
131 Hassanain, 2012). The upper part of the pre-rift succession comprises of fine-grained basinal
132 carbonates (Thebes, Darat and Tanka Formation) that are unconformably overlain by early syn-rift
133 mixed carbonate and siliciclastic sediments of the Tayiba and Abu Zenima Formation (Jackson *et al.*,
134 2005).

135 The primary focus of this study, the early Eocene Thebes Formation, has been informally subdivided
136 into the lower and upper Thebes, comprising eight lithofacies (Fig. 2; Table 1). The lower Thebes Fm.
137 is composed of skeletal packstone (S1) in which four remobilised facies are embedded (Hirani, 2014):

- 138 • Lenticular-shaped matrix-supported and clast-supported conglomerates (R1) with convex
139 upper contacts. These bodies form along depositional dip and are up to ~250 m long, < 65 m
140 wide and up to ~20 m thick and are interpreted as debrites.
- 141 • Upward-fining formainiferal grainstones (R2) that are up to 100 m in length and < 50 m wide
142 and < 6 m thick often overlying R1 facies, which are interpreted as turbidites.
- 143 • A single, thin (< 2 m thick) sheet-like bed of matrix-supported conglomerate (R3) with a
144 scoured base which can be traced for up to 1.5 km along strike and 1 km down-dip towards
145 the top of the lower Thebes member. It is interpreted to have formed by shelf margin or upper
146 slope collapse.
- 147 • The transition between the upper and lower Thebes Fm. is characterised by a slumped
148 skeletal grainstone (R4) which is < 3 m thick and up to 5 m long and is interpreted to have
149 formed by plastic flow.

150 The upper Thebes Fm. dominantly comprises skeletal wackestones (B1) with abundant planktonic
151 foraminiferal wackestone facies that are characteristic of low energy, pelagic deposition in a deep
152 marine environment. They are interbedded with massive skeletal grainstone beds (R5), sometimes
153 with channelized bases (R6). Overall, the Thebes Fm. is interpreted as an upward-deepening
154 succession that was deposited on an unstable slope and an outer ramp – basinal environment.

Methodology

Field, petrographical and petrophysical methods

The stratigraphic distribution of the dolostone bodies and their geometries were determined by field mapping and logging supported by Google Earth © images. Detailed stratigraphic logs were collected and comprehensively sampled within the dolostone bodies, host limestone and the contact zones at the margins of the dolostone bodies. Fracture data was collected along more than 50 scanlines from both limestone and stratabound dolostone beds. The data recorded for each scanline included fracture type, orientation, intensity (number of fractures per meter) and termination and has been detailed in Korneva *et al.*, 2017.

Thin and polished sections were prepared from 219 samples, following impregnation with blue-dye resin and staining with alizarin Red S and potassium ferricyanide to constrain the mineralogy (Dickson, 1966). All thin sections were analysed using standard petrographic methods (transmitted light with cold cathode luminescence microscopy), with limestone textures described using the Dunham (1962) classification and dolostone textures described using the Sibley and Gregg (1987) classification. The burial history curve for the lower Thebes Fm. in the footwall of the Hammam Faraun Fault (HFF) was constructed using the present-day thickness of the sediments overlying the Thebes Fm., with tie points at various points throughout the syn-rift stratigraphy (Armstrong 1997; Gawthorpe *et al.*, 2003; Woodman 2009).

Standard helium porosity measurements were performed on 44 plugged samples with 1-inch diameter core plugs of variable length using a digital helium porosimeter (DHP 100), Permeability was measured using N₂ gas under a series of pressure conditions using a digital gas permeameter (DHP 200) to determine the standard Klinkenberg permeability, reported as millidarcy (mD).

Geochemistry

All geochemical data is summarised in Table 2. Powdered samples were obtained using a dentist drill. Bulk mineralogy and stoichiometry were determined by XRD analysis, using the Lumsden (1979) equation to determine the measured d[104] spacing ($M = 333.3 \times d\text{-spacing} - 911.99$). Inductively-coupled plasma mass spectrometry (ICP-MS) and Inductively-coupled plasma atomic emission spectrometry (ICP-AES) were used to quantify the concentrations of minor and trace elements (Fe, Mn, Al, Sr, Ni, Ba) within 18 representative samples, reported in ppm. Rare Earth Element (REE) analysis was conducted on 16 representative samples at the French Research Institute for Exploitation of the Sea (Laboratoire Géochimie et Métallogénie), using the methodology outlined by Bayon *et al.*, (2009). The REE concentrations were normalized to the post-Archean Australian Shales (PAAS) for comparison with previous studies using REE seawater proxies (Nance and Taylor, 1976; Haley *et al.*, 2004; Nothdurft *et al.*, 2004).

C and O isotope ratios were collected at the SUERC research facility (East Kilbride, Scotland) using the carbonate CO₂ extraction line. The samples were analysed using the method outlined by (McCrea, 1950), where 7 mg of powdered sample was digested in 100% phosphoric acid in a 25°C water bath (calcite samples left to react for 3 hours and dolomite samples for 24 hours). The resulting CO₂ gas was analysed on a VG OPTIMA mass spectrometer. All stable isotope values are reported in per mil (‰) relative to the Vienna Pee Dee Belemnite (VPDB) standard. A marble standard was used to calibrate the results, as well as replicate analyses, which were reproducible to ±0.1‰ (2σ). The oxygen isotopic data was adjusted for isotopic fractionation associated with the phosphoric acid reaction using the Rosenbaum and Sheppard (1986) calibration.

Strontium isotope analyses were undertaken at the French Research Institute for Exploitation of the Sea (Laboratoire G ochimie et M tallog nie). The carbonate powders were weighed and dissolved in 3M HNO₃. After reacting, the liquid was heated on a hot plate to evaporate and eliminate excess ions and re-dissolved in 3M HNO₃. The sample was purified using Sr spec extraction chromatic resin and Sr column preparation followed the procedure of Horwitz and Bloomquist (1975). The Sr was collected and analysed using the Triton Thermal Ionization Mass Spectrometer, with precision of individual runs at 0.000005 (1σ). All results are reported to the NBS 987 standard.

Clumped isotope analysis was carried out on 3 dolomite samples at the Qatar Stable Isotope Laboratory at Imperial College London. Procedures followed Dale *et al.* (2011). Briefly, three replicate measurements were done per sample, with replicates measured after a month to correct for errors over time. For each replicate measurement, 5 mg of powdered sample was digested and reacted in 2 ml of 104% phosphoric acid at 90°C for 20 minutes. The resulting CO₂ gas was purified in a manual vacuum line through a poropak column and analysed on a MAT 253 mass spectrometer to simultaneously measure Δ_{47} , $\delta^{18}\text{O}$ and $\delta^{13}\text{C}$. Data correction were done using Easotope (John and Bowen, 2016): non-linearity corrections were applied using the heated gas method (Huntington *et al.*, 2009), and the acid fractionation factors for Δ_{47} were applied using Guo *et al.* (2009). All values are reported in the absolute reference scale of Dennis *et al.* (2011; Carbon Dioxide Equilibrated Scale, or 'CDES'), using the following standards for the conversion: heated gas (0.027‰ CDES, Wang *et al.*, 2004), ETH3 (0.700‰ CDES, Meckler *et al.*, 2014) and Carrara marble (ICM, 0.399‰ CDES, Dale *et al.*, 2014). The Δ_{47} values were converted into a temperature using the Kluge *et al.* (2015) calibration, and errors are reported as ±1S.E., corresponding to a confidence interval of 68%. To calculate the $\delta^{18}\text{O}$ of the dolomitizing water, we used the dolomite-water fractionation equation from Horita (2014).

Mass balance calculation

In order to calculate the number of moles of dolomite per m³ of stratabound dolostone, an average porosity of 19% was assumed based on an average present-day porosity of 13% plus an average 6% to account for porosity occluded by telogenetic cements. The input and output data for the mass

balance calculation are shown in Table 5. For dolomite with a density of 2.84 g/cm^3 and a molar weight of 184.4 g , 1 m^3 of dolostone contains some 12500 moles of dolomite ((density /molecular weight) * (1- fractional porosity)). Mass balance calculations provide a minimum estimate of the total volume of fluid required to dolomitize the observed volume of stratabound dolostone based on this molar concentration of dolomite. The dolomitizing fluid is assumed to derive from Eocene-Oligocene seawater, the chemistry of which was calculated using PHREEQC (Parkhurst and Appelo, 2013) based on compositional data in Brennan *et al.* (2013). This seawater has a salinity of 33.8‰ , a density at 25°C of 1021 kg/m^3 and concentrations of calcium and magnesium of 16 and 36 ppm respectively. We use the Pitzer database (Plummer *et al.*, 1988), which takes into account specific ion interactions that occur in high ionic strength solutions (Krumgalz, 2001). The dolomitization potential is the volume of fluid required to dolomitize 1 m^3 of limestone, and was derived from the mass of dolomite estimated by PHREEQC to precipitate from the solution in the presence of excess calcite. From the minimum total volume of fluid required, the minimum flux based on the estimated range of the age of dolomites from field relationships and strontium isotope data is estimated. Sensitivity to both temperature, using constraints from clumped isotope paleo-thermometry, and the degree of evaporative concentration of the Eocene-Oligocene seawater, based on the $\delta^{18}\text{O}$ of the dolomitizing fluid were also investigated.

Field observations

The Thebes Formation is partially dolomitized in the footwall of the HFF (Fig. 3). The dolostone bodies are easily identified by their distinctive dark brown weathering colour, relative to the cream colour of the host limestone. Two main types of dolostone bodies have been observed in the field (Fig. 4):

- a) Stratabound dolostone bodies, varying in length from 5 m up to 300 m along depositional dip, and ranging in thickness between 25 cm and 5 m. These dolostone bodies extend for up to 2 km away from the HFF, before disappearing beneath the sedimentary cover.
- b) Massive dolostone bodies, up to 500 m wide (distance from HFF) and 60 to 80 m thick. Dolostone tongues associated with these massive bodies extend for up to 100 m away from the massive dolostone bodies, forming 1 to 5 m thick bands (Hirani, 2014; Hollis *et al.*, 2017).

This paper focuses on the stratabound dolostone bodies and the major controls associated with their formation. Stratabound dolostone is restricted to the lower Thebes member (Fig. 2B), forming only within the debrite (R1) and turbidite (R2) facies. Debrite and turbidite facies may be completely dolomitized, or the dolostone bodies may terminate within them (Fig. 4). There was no evidence in the field for a sedimentological control on the distribution of dolostone within facies R1 and R2, and no consistent observations to suggest a geological control on the termination of dolostone. The dolostone bodies are offset by the Gebel Fault, by approximately 300 m (Fig. 3). The dolomitized beds are often more prominent within the landscape than the limestone as they are more resistant to

weathering. The upper and lower contacts of these bodies with the adjacent limestone are usually sharp and planar, with abrupt lateral terminations (Fig. 4).

Both limestones and stratabound dolostones are affected by bed-bound, bed-perpendicular joints that strike NW-SE and NNE-SSW. Fracture density for all lithofacies shows a positive correlation with bed thickness, with the highest density (narrowest fracture spacing) noted in the slope packstones (S1). The matrix-supported conglomerates (R1) have a fracture density that is only slightly lower than that in the packstones, while the lowest fracture density is noted within the turbidite grainstones (R2) (Korneva *et al.*, 2017).

Pre-dolomitization diagenesis and geochemistry

The texture and geochemical signature of the precursor limestone was described to determine the likely controls of rock reactivity and petrophysical properties on the distribution of dolostone. A large proportion of the slope and remobilised deposits have been recrystallised by microcrystalline calcite (Fig. 5A), with little evidence of recrystallization of the basinal wackestone facies (Fig. 5B). From herein, the basinal wackestone facies are referred to as unaltered limestones, and the slope and remobilised deposits are referred to as recrystallised limestones.

The rare-earth element (REE) signatures of 3 unaltered limestone and 4 recrystallised limestone samples exhibit positive La and negative Ce anomalies. They are also relatively enriched in the heavier rare earth elements (HREE), although the increase in the concentration of the HREE is suppressed in the recrystallised limestone (Fig. 6A). Whole rock isotopic values for the unaltered limestones average $\delta^{18}\text{O} = -3.35\text{‰ VPDB}$ and $\delta^{13}\text{C} = -0.17\text{‰ VPDB}$ whilst the recrystallised limestones exhibit lower $\delta^{18}\text{O}$ values (mean = -6.4‰ VPDB ; -5.12‰ VPDB to -7.80‰ VPDB) (Fig. 7A). The $\delta^{13}\text{C}$ values for the unaltered limestone (mean = -0.2‰ VPDB ; -1.0‰ VPDB to $+0.7\text{‰}$) and the recrystallised limestone have a similar range (mean = 0.4‰ VPDB ; -0.69‰ VPDB to $+1.04\text{‰ VPDB}$). The $^{87}\text{Sr}/^{86}\text{Sr}$ ratio of 1 unaltered limestone sample is 0.707814 while the recrystallised sediments are more enriched (mean = 0.707849; 0.707773 to 0.708011; Table 2).

Dolostone macroscale features

The stratabound dolostone bodies occur almost exclusively within the matrix-supported debrite facies (R1) and, to a lesser extent, the turbidites (R2) (Fig. 8F). They typically exhibit fabric preserving textures, with a dark grey dolomitized matrix surrounding dolomitized clasts with a distinctive rusty brown colour (Fig. 8A). Locally, dolomitized clasts within the debrites (R1) are wrapped by zebra-like fabrics (Fig. 8B), which can also occur in random orientations within the dolostone strata, often beneath chert nodules. These visually striking fabrics are made up of alternating bands (2-4 mm thick) of dolostone, with elongated vuggy pores that are partially cemented by coarsely crystalline calcite

cements (Fig. 8C) and, occasionally, gypsum. In addition, vugs and mouldic pores after clasts are often occluded by coarsely crystalline calcite cements with botryoidal, fascicular and dogtooth morphologies (Fig. 8D and 8E). These cements have depleted $\delta^{13}\text{C}$ (-6.1‰ VPDB , -3.6 to -10.1‰ VPDB) and $\delta^{18}\text{O}$ (-11.1‰ VPDB ; -5.1 to -16.8‰ VPDB). Iron and sulphate rich minerals, including haematite and gypsum, post-date the pore filling calcite cements.

Dolostone microscale textures

In thin section, the matrix of the stratabound dolostone bodies exhibit both planar-s and non-planar textures (Sibley and Gregg, 1987; Fig. 9). The planar-s textures have a cloudy core and some have clear rims (CCCR), ranging in size between 20 and 60 μm , with minor fabric preservation evident as ghosts of *Nummulites*. Under cathodoluminescence (CL), they exhibit zoned luminescence, with mottled bright red and orange luminescent cores, an intermediate thick dull green to yellow luminescent zone and a thin bright red luminescent outer zone (Fig. 9B). The non-planar dolomite textures are composed of very cloudy crystals between 10 and 30 μm in size with no evidence of fabric preservation (Fig. 9C). These dolomites are not zoned in CL, with mottled bright red and orange luminescent crystals.

Dolomitized clasts within the stratabound dolostone bodies comprise 75-150 μm CCCR dolomite crystals with a planar-s texture. Overall, the dolomitization is non-mimetic, but some precursor limestone texture is preserved as ghosts of benthic foraminifera. The contact between the clast and matrix is characterised by an irregular corrosion rim in which the dolomite crystal cores appear to be preserved relative to the crystal rims (Fig. 10A). Under CL, clast-replacive dolomite has bright red and orange mottled luminescent cores with dull orange luminescent outer zones (Fig. 10B). The matrix adjacent to the clasts has a cloudy, non-planar texture with rhombic crystals ranging in size between 50-80 μm that are predominantly non-luminescent with patches of bright red and orange luminescence.

Dolostone geochemistry

The geochemical composition of the stratabound dolostone bodies is summarised in Table 2. X-ray diffraction analysis confirms the mineralogy to be stoichiometric dolomite (mean $\text{CaCO}_3 = 51.3\%$; 50.0-55.5%) with up to 5% calcite in some samples, and minor quantities of non-carbonate phases including quartz and gypsum. Rare Earth Element analysis of 9 dolomite samples reveals a positive La and negative Ce anomaly, with a decrease in the concentration of the HREE giving a flattened profile compared to unaltered limestone (Fig. 6A). All samples cluster tightly within the marine quadrant of a Pr/Pr^* ($[\text{Pr}/(0.5\text{Ce} + 0.5\text{Nd})]_{\text{SN}}$) versus Ce/Ce^* ($[\text{Ce}/(0.5\text{La} + 0.5\text{Pr})]_{\text{SN}}$) plot (Bau and Dulski, 1996; Webb and Kamber, 2000; Fig. 6B). $^{87}\text{Sr}/^{86}\text{Sr}$ ratios are more radiogenic than that of the unaltered limestone and range between 0.707992 and 0.708241, coincident with Oligo-Miocene

seawater (Table 2; Fig. 11). Concentrations of Fe (mean = 151 ppm; 37-411 ppm) and Sr (mean = 142 ppm; 59-232 ppm) are moderate, whilst Mn concentrations are enriched (mean = 463 ppm; 208-991 ppm) (Table 2).

The $\delta^{18}\text{O}$ composition of the stratabound dolostones is constrained to a range of -4.0‰ VPDB to -8.0‰ VPDB (mean = -5.5‰ VPDB); $\delta^{13}\text{C}$ values range from -1.4‰ VPDB to $+1.2\text{‰ VPDB}$ (mean = -0.1‰ VPDB) (Fig. 7A; Table 2). The estimated temperature by clumped isotope paleo-thermometry (Table 3a) overlaps at the 68% confidence level for the three samples in a range of $69\text{--}78^\circ\text{C}$ (Fig. 7C). Using these temperatures, $\delta^{18}\text{O}_{\text{dolomite}}$ and the dolomite-water fractionation equation of Horita (2014), the fluid composition for the three samples at the 68% confidence level is $+2.5 \pm 0.1\text{‰}$ (Fig. 7C).

Petrophysical properties

Overall, porosity is higher in the unaltered limestones (average 13%, range 1 – 39%; Table 1) than in the dolomitized facies (average 3%, range 1-7%) whilst permeability is uniformly low (average 0.47mD , range $0.01\text{--}3.5\text{mD}$ in limestone; average 0.1mD in dolostones, with all values $<2\text{mD}$; Table 1). Within the limestones, the best porosity is within basinal wackestone facies (B1 average = 24%) and the channelized grainstone facies (R6 average = 18%). Pore types include interparticle and mouldic macropores and intraparticle microporosity. Dolomitized facies are dominated by intercrystalline macro- and micropores in thin section but also exhibit large vugs (10-30 cm diameter) and sub-spherical mouldic pores after clasts (5-20 cm diameter) which were too large to sample for core analysis.

Interpretation

Timing of limestone recrystallisation

To constrain the composition of the dolomitizing fluids, it is necessary to consider the composition of the precursor limestone, since the geochemical fingerprint of the stratabound dolostone could be inherited from the host rock (e.g. Banner *et al.*, 1988). The $^{87}\text{Sr}/^{86}\text{Sr}$ ratio of the unaltered and recrystallised limestones is less radiogenic than the stratabound dolostone, and coincides with late Eocene seawater (Koepnick *et al.*, 1985; Fig. 11). The $^{87}\text{Sr}/^{86}\text{Sr}$ ratio for the unaltered limestone samples would be expected to match Early Eocene seawater, and the slightly younger age may either reflect minor recrystallization that is not visible petrographically or contamination by later-precipitated calcite cements. The unaltered limestones have a REE signature that is typical of seawater, with a positive La and negative Ce anomaly, as well as relative enrichment in the heavier rare earth elements (HREE) (Nothdurft *et al.*, 2004; Wyndham *et al.*, 2004). Whole rock isotopic values for the unaltered limestones lie within the range that is expected for deposition from Eocene seawater (Pearson *et al.*, 2001). Recrystallised limestones also display a positive La and negative Ce anomaly, but with slightly depleted REE concentrations (Fig. 6A). Their $\delta^{13}\text{C}$ signature is similar to that of the unaltered

limestones, however they have a significantly depleted $\delta^{18}\text{O}$ (mean = -6.4‰ VPDB compared to -3.6‰ VPDB for unaltered limestones). Assuming recrystallization from seawater, estimated as $\delta^{18}\text{O}_{\text{SMOW}} = -1$ to -0.75‰ for early-mid Eocene seawater (Pearson *et al.*, 2001) and using the fractionation equation of Friedman and O'Neil (1977), this would equate to temperatures of $\sim 42^\circ\text{C}$. Based on a normal geothermal gradient of $25^\circ\text{C}/\text{km}$ and a seawater temperature of 25°C , this temperature could have been reached at $<750\text{m}$ burial. In this case, the depleted HREE signature could be a result of mineral stabilization under suboxic conditions (Haley *et al.*, 2000; Melim *et al.*, 2002).

Timing of dolomitization

Field relationships indicate that stratabound dolostone bodies are offset by the Gebel Fault, which became inactive prior to the rift climax, indicating that dolomitization must have occurred before the mid-Miocene ($\sim 15\text{--}17\text{ Ma}$; Fig. 12; Gawthorpe *et al.*, 2003). Dolomitization is therefore constrained to post-deposition (35 Ma) and pre- 15 Ma . It seems unlikely that dolomitization was pene-contemporaneous with sedimentation on the HFF block because deposition during the Eocene took place in a deep-water basin (Moustafa and Abdeen, 1992), an environment that is not normally associated with dolomitization. Furthermore, the abundance of stratabound dolostone decreases with distance from the HFF, which was not initiated until 26 Ma (rift initiation), rather than along depositional dip; indeed no stratabound dolostone is seen down-dip of the study area, to the south (Hirani, 2014). It is unlikely that up-dip dolomitization occurred as only a very minor volume of dolostone is described from platform top and upper slope facies in age-equivalent, proximal sediments outcropping in the Northern Galala Plateau (Hontzsch *et al.*, 2011). Furthermore, no clasts of dolomitized limestone are found within otherwise undolomitized remobilized facies, ruling out the possibility that dolomitization in the field area is a down-dip extension, or remobilisation of, dolomitization on the platform top. Since deposition of deep water (outer neritic), slope-basinal limestone persisted into the late Eocene (Tanka Formation; Fig. 1; Jackson *et al.*, 2006), dolomitization at any point in the Eocene is considered highly unlikely. This constrains formation of the stratabound dolostone to the Oligo-Miocene ($\sim 26\text{--}15\text{ Ma}$), a period of $\sim 10\text{ My}$ that was coincident with rift initiation, but predated the rift climax.

Origin and temperature of dolomitizing fluids

Stratabound dolostone is stoichiometric and exhibits planar-s and non-planar textures. Although crystal texture is not an unequivocal indicator of the temperature of dolomitization, the presence of both fabrics would suggest that fluid temperatures ranged from just below to a little above the critical roughening temperature of 55°C (Sibley and Gregg, 1987). The mottled orange and red luminescent cores observed in CL (Fig. 9B) may represent remnants of the host limestone, perhaps due to rapid nucleation during the earliest stages of dolomitization. The clear rims that surround the core have a well-defined concentric zonation under CL, typical of a slower rate of growth as the crystal passively

filled interparticle porosity. The ratio of Mn to Fe, based on mean values of Mn (469 ppm) and Fe (140 ppm) is high (3.35), suggesting luminescence is activated by Mn incorporated into the lattice under suboxic conditions from a fluid with low concentrations of Fe. Zonation would then most likely occur as a result of changes in the concentration of trace elements during crystal growth (Brand and Veizer, 1980; Machel and Burton, 1991). The thick, dull green to yellow luminescent zones within the planar-s dolomite could be activated by higher concentrations of REE (Machel and Burton, 1991) or Mn^{2+} substitution for Ca^{2+} within the crystal lattice (Gillhaus *et al.*, 2010).

The $^{87}\text{Sr}/^{86}\text{Sr}$ ratio of the stratabound dolostone coincides with late Oligocene to early Miocene seawater (0.708062 to 0.70824; Koepnick *et al.*, 1985; Jones *et al.*, 1994; Reilly *et al.*, 2002; Fig. 11). Average concentrations of Sr are 142 ppm, with the lowest concentrations (59 ppm) in the most stoichiometric dolomite and increasing Sr concentration with decreasing dolomite stoichiometry (Fig. 6C). Based on Tertiary dolostones formed from seawater, Vahrenkamp and Swart (1990) noted that Sr concentrations increase as dolomite stoichiometry decreases, since Sr is preferentially hosted in the calcite lattice; our results are consistent with their observations. The relatively low concentrations of Fe (< 500 ppm; Table 2) within the stratabound dolostones and average $\delta^{13}\text{C}_{\text{dolomite}} = -0.1\text{‰ VPDB}$ are also consistent with formation from seawater ($\delta^{13}\text{C} \sim 0\text{‰}$; Prokoph *et al.*, 2008). However, $\delta^{13}\text{C}$ has a slightly wider range (-1.4 to 1.2‰ VPDB) than the unaltered and recrystallised limestones (Fig. 7A; Table 2). The REE profile of dolostone shows that the HREE are slightly suppressed compared to unaltered and altered limestone, although they cluster in the marine quadrant of the Pr/Pr* vs Ce/Ce* plot (Fig. 6B). Typically, $\delta^{13}\text{C}$ and REE profiles are inherited from the precursor limestone under all but the highest fluid-rock ratios ($\sim 1:10^4$; Banner *et al.*, 1988). The subtle differences between the host limestone and stratabound dolostone in this dataset suggest that fluid-rock ratios could have been high enough for the compositional signature of the dolomitizing fluid to be retained.

The $\delta^{18}\text{O}_{\text{dolomite}}$ measured by conventional analysis have tightly clustered values (mean = -5.5‰ VPDB; median = -5.6‰ VPDB; mode = -6.5‰ VPDB). From the three clumped isotope analyses, $\delta^{18}\text{O}_{\text{water}}$ ranges from +0.6 to +3.6‰. Applying these data to the conventional isotope data (Table 3b) and the dolomite-water fractionation equation of Matthews and Katz (1977), dolomitization from the lightest fluid, which approximates penecontemporaneous seawater (+0.6‰), would occur at 36 °C to 61 °C. This assumes lower temperatures than calculated by clumped isotope analysis (Table 3b). However, if dolomitization was from a heavier fluid (+3.6‰), fluid temperatures are calculated as 54 – 83 °C; *i.e.* closer to the range of clumped isotope-determined temperatures. In reverse, using the clumped isotope temperatures to calculate the oxygen isotopic composition of the dolomitizing fluid from the mean $\delta^{18}\text{O}_{\text{dolomite}}$ of the conventional data ($\delta^{18}\text{O}_{\text{dolomite}} = -5.5\text{‰ VPDB}$; Table 3b) gives $\delta^{18}\text{O}_{\text{water}} = +4$ to +5‰ SMOW.

Consequently, although strontium isotope and trace element data are consistent with dolomitization from seawater, oxygen isotope data suggests dolomitization occurred from an oxygen-isotopically

enriched fluid. This could occur if seawater was slightly evaporated. Using the technique of Swart (1989) and assuming a $\delta^{18}\text{O}_{\text{seawater}} = +0.6\text{‰}$, $\delta^{18}\text{O}_{\text{water vapour}} = -2\text{‰}$ (equivalent to modern day rainfall within the study area) and a humidity of 50% (equivalent to the modern day), evaporation of a 30% fraction of seawater would form a fluid with $\delta^{18}\text{O}_{\text{water}} = +5.5\text{‰}$ and a salinity of 48 ppt. With an increasing fraction (40 to 50%) of evaporation to a fluid of 56‰ to 68‰ salinity, the $\delta^{18}\text{O}_{\text{water}}$ decreases to +3.0‰ and +2.0‰ respectively (Table 4). A mixed carbonate-clastic Oligocene succession on the HFF block records deposition within a shallow water coastal environment (Jackson *et al.*, 2006). Evaporites have not been described, but given a palaeo-latitude similar to today, and therefore an arid to semi-arid climate, it is possible that seawater was mesohaline, and therefore a 30% evaporated fraction of seawater seems reasonable. The stratabound dolostone bodies are consequently interpreted to have formed from slightly evaporated (mesohaline) seawater, at temperatures up to ~80°C, during the Oligocene to early Miocene, prior to movement on the Gebel Fault and onset of the rift climax. This interpretation is evaluated further in the discussion.

Mass Balance

In order to calculate the volume of seawater required for formation of the stratabound dolostones, we consider a 1 m wide slice of the 200 m thick lower Thebes member within which the stratabound dolostone bodies extend for a distance of 2000 m perpendicular from the HFF (Table 5). The distribution of dolostones could only be viewed in the field in pseudo-3D, but based on field logs, photos, mapping and modelling they were estimated to comprise 19% of the total rock volume. This gives an estimated volume of 400 000 m³ carbonate per 1 m wide section with approximately 76,000 m³ dolostone. An equal volume can be assumed in the hanging wall, even though this cannot be observed as the hanging wall is offshore and displaced vertically from the footwall by several kilometres.

The calculated temperature of dolomitization based on mean $\delta^{18}\text{O}_{\text{dolomite}}$ and assuming a fluid of +3.6‰_{SMOW} is 64°C. Assuming dolomitization by Oligo-Miocene seawater at 65°C, up to 1.30×10^{-2} moles of dolomite can form from each Kg of seawater. Thus 77 Kg of seawater (ie. 0.01 moles/kg), or 0.077 m³ is required to precipitate 1 mole of dolomite. At an estimated porosity of 19% the stratabound dolostone bodies are comprised of 12475 mol dolomite / m⁻³, so multiplying by 0.077 m³/mol gives a minimum of 957 m³ of Oligo-Miocene seawater to precipitate 1m³ of dolomite at 65°C. Multiplying by the total volume of dolostone gives 72, 725, 808 m³ fluid necessary to dolomitize each 1m slice of the footwall. Assuming a maximum dolomitization period of 10 My (i.e. from rift initiation to cessation of movement on the Gebel Fault), then a minimum flux of 7.27 m³ per year would be required into the lower Thebes footwall for each 1 m wide section of the fault, with at least an equivalent flux into the hanging wall. Assuming that porosity was 19% and entirely effective, this gives a velocity of at least 77 m/yr within the fault, and a lateral flux of at least 1.0 m/year.

Considering mesohaline brines formed from Oligo-Miocene seawater at concentration factors of between 1.43 and 2 increases the dolomitization potential at 65°C to 0.02 and 0.03 moles of dolomite

respectively. This reduces the volumetric requirement, suggesting minimum fluid fluxes within the fault of 53.97 and 38.13 m/yr, equivalent to lateral fluxes of only 0.70 and 0.49 m/yr. At 80°C, although kinetics may favour more rapid dolomitization, the dolomitization potential is actually lower, with a reduction in the moles of dolomite formed per Kg by a factor of 0.76 to <0.02 mols per kg, compared to 65°C, independent of the degree of evaporative concentration (Table 5). The estimated fluid flow rates both within the fault and within the lower Thebes Formation (~1 m/yr) are rather low compared with those in modern active hydrothermal systems (1000 m/yr) and modern confined aquifers (1 to 30 m/yr) (Giles, 1987), but are consistent with rates calculated by Corbella *et al.* (2014) for a similar system. Also, rather than a steady flow system operating over 10 My, it is likely that significantly higher flow occurred over numerous shorter periods associated with transient increases in fault zone permeability.

Post-dolomitization diagenesis

The stratabound dolostone bodies contain localised vugs and zebra-dolomite like features which are occasionally occluded by botryoidal, fascicular and dogtooth calcite (Fig. 8C and 8D). The zebra-like fabrics are highly localised, often beneath chert clasts and are strikingly different from 'typical' zebra dolomite fabrics (e.g. Davies and Smith, 2006) because they lack saddle dolomite cements. There are many theories to explain the formation of zebra dolomite, but the absence of a relationship to facies and the absence of pressure solution features suggest that they may have formed under elevated pressure and perhaps transtension (e.g. Lopez-Horgue *et al.*, 2009; Juerges *et al.*, 2016). It is very tentatively suggested that such conditions occurred during the late syn-rift when movement on the HFF waned in response to movement along the Aqaba- Levant transform (Montenat *et al.*, 1988; Bosworth *et al.*, 2005). At this point, dolomitization along the HFF is interpreted to have stopped (Hollis *et al.*, 2017) and therefore perhaps a limited flux of dolomitizing fluids inhibited cementation of the zebra-like fabrics by dolomite.

Continued uplift and rotation on the HFF from the Miocene to Recent has brought the HFF block to surface (Fig. 12). During this time, the Thebes Formation re-entered the marine realm before it became emergent. Calcite cementation could have occurred within vugs at this time. Some textures (e.g. botryoidal calcite) are suggestive of marine cementation, but the highly depleted carbon and oxygen isotopic values measured in these cements are suggestive of cementation by, or recrystallization from, meteoric fluids. Locally, this has also resulted in patchy dedolomitization of stratabound dolostone (Hirani, 2014).

Discussion

Dolomitization mechanism

The decrease in the volume of stratabound dolostone away from the HFF suggests that this major, crustal-scale fault played an important role in controlling the flow of dolomitizing fluids into the Thebes Fm. Dolomitization is interpreted to have occurred from seawater or slightly ($\leq 2\times$) evaporated

seawater prior to the rift climax, when deformation became focused on the HFF, and before termination of movement on the Gebel Fault (i.e. before 15 Ma). At this time, the base of the Thebes Formation was at a burial depth of ~700 m (early Oligocene) to ~850m, when movement on the Gebel Fault was initiated (Fig. 12). Clumped isotope data indicates that dolomitization occurred at temperatures of 67-78°C. Consequently, if dolomitization was from seawater, then that seawater must have descended, heated and circulated towards and along the HFF before it breached the surface (Fig. 13).

From the early Oligocene, a series of incipient intrablock faults across the study area controlled the distribution of shallow marine sediments of the Tayiba Fm. (Early to Middle Oligocene), indicating that the proto-HFF footwall was flooded (Refaat and Imam, 1999; Jackson *et al.*, 2006). Where these intraplateau faults breached the surface, they could have acted as conduits for the drawdown and circulation of seawater. The low permeability of the underlying Mesozoic and Tertiary succession could have maintained seawater circulation along the fault plane to depth. On reaching the highly permeable Nubian Sandstone Formation (Fig. 13), however, seawater could have been entrained within geothermal convection cells. Down depositional dip, fluids would have encountered the proto-HFF, where they could have discharged. Elevated heat flux associated with rift initiation would have both heated fluids and provided a conduit for egress of buoyant fluids through the proto-HFF (Fig. 13). Jackson *et al.* (2005) indicate that the tip of the HFF and steeply dipping normal fault splays developed in the Thebes Formation during rift initiation, and this would have allowed fluids to migrate into both the proto- hanging wall and footwall within the Thebes Formation. This would have been facilitated by an order of magnitude permeability contrast between the Thebes Fm. and the bounding formations. Flux may have been further enhanced by development of a narrow damage zone in proximity to the evolving HFF.

Such a conceptual model is not without precedent. Pearson and Garven (1992) modelled fluid flow within continental rift basins, and noted draw-down of fluids at fault escarpments with discharge in the centre of the rift. Jones and Xiao (2013) also modelled downward fluid flux along faults as controlling carbonate dissolution and cementation within pre-rift lacustrine carbonates, with more extensive carbonate dissolution in the vicinity of faults, where fluid is drawn down, and cementation where hot fluids are vented to the surface. Much of this previous work is model-based, however, and has only been considered and applied in a few field studies. For example, using field, petrographical and geochemical proxies, Rusticelli *et al.* (2016) and Wilson *et al.* (2007) proposed dolomitization from seawater drawn down surface-breaching faults, whilst Corbella *et al.* (2014) modeled basin-scale convection of seawater down faults and via a fractured basement, constrained by field observations and geochemistry. It is likely, therefore, that the conceptual model we present for fault-controlled fluid flux is more common than has been recognized within the literature. The limited number of examples perhaps reflects the fact that many case studies of fault-controlled dolomitization are in older sediments that have been overprinted by later phases of dolomitization (Hollis *et al.*, 2017). However,

the paucity of case studies that infer down-fault circulation of seawater could also reflect the persistence of a conceptual notion whereby fluid circulation is only interpreted to occur up faults. It is therefore highly likely, since many rift basins evolve through the localization of deformation from numerous small faults to a single, deep-seated crustal lineament, that similar patterns of down-fault fluid flow and geothermal convection occurs on many carbonate platforms in extensional basins.

Implications to the composition of dolomitizing fluids

Seawater is the most volumetrically abundant Mg-enriched fluid for dolomitization. On geochemical evidence, it has been argued that stratabound dolomitization on the HFF took place from slightly evaporated seawater. Given that we propose geothermal convection of seawater via a basal clastic aquifer, the potential for modification of seawater during fluid migration has to be considered. In particular, fluid-rock interaction within the Nubian Sandstone aquifer, where fluid residence times were high, could have modified $\delta^{18}\text{O}_{\text{water}}$, $^{87}\text{Sr}/^{86}\text{Sr}$, and trace element compositions. Both REE profiles and $\delta^{13}\text{C}$ imply high water-rock ratios, and so any modification of seawater composition would have required significant fluid-rock interaction. The Nubian Formation is dominated by quartz arenites (Pomeyrol, 1968; Weissbrod and Nachmias, 1986; Nabawy *et al.*, 2009), however, offering little opportunity for isotopic or trace element enrichment. Importantly, the concentration of Sr relates strongly to dolomite stoichiometry, suggesting that any apparent enrichment in Sr is a result of a higher concentration of Ca (Fig. 6C). Indeed, if $^{87}\text{Sr}/^{86}\text{Sr}$ had been enriched, then the actual age of dolomitization must be older than the apparent (Oligo-Miocene) age since the $^{87}\text{Sr}/^{86}\text{Sr}$ of post-Miocene seawater is more enriched than the values measured for the stratabound dolostones (Fig. 12). Given the narrow constraints on the timing of dolomitization (26-15 Ma) from field relationships, and an absence of evidence for pre-Oligocene dolomitization, it seems unlikely that this is the case.

Mid Ocean Ridge basalts have differentially been reported as both a source and a sink for Mg in seawater (Ligi *et al.*, 2013). Hence, it is possible that Mg-enrichment of Oligo-Miocene seawater occurred during fluid interaction with basaltic dykes and sills emplaced during rift initiation in proximity to the HFF, and in the Northern Gulf Basaltic Province (22-26 Ma; Monténat *et al.*, 1986; Moustafa and Abdeen 1992; Patton *et al.*, 1994; Bosworth, 2015). A linear mixing of > 50% seawater ($\delta^{18}\text{O}_{\text{water}} = 0.6\text{‰}$ and $\delta^{13}\text{C}_{\text{water}} = 0\text{‰}$) with a magmatic fluid of $\delta^{18}\text{O}_{\text{water}} = +7\text{‰}$ and $\delta^{13}\text{C}_{\text{water}} = -7\text{‰}$ would result in a fluid with $\delta^{18}\text{O}_{\text{water}} = 0$ to $+3.5\text{‰}$ and $\delta^{13}\text{C}_{\text{water}} = -3.5$ to 0‰ (Zheng and Hoefs, 1993), close to values determined for the stratabound dolostone. Normally, magmatic fluids are depleted in $^{87}\text{Sr}/^{86}\text{Sr}$, however Bosworth *et al.* (2015) measured enrichment in radiogenic strontium, uranium and lead as well as low concentrations of MgO (5.6-6.3 wt%) in the basalts from the Northern Gulf Basaltic Province. Consequently, enrichment in $^{87}\text{Sr}/^{86}\text{Sr}$ might have occurred as a result of seawater mixing with magmatic fluids, but this would mean that the actual age of dolomitization is older than interpreted, which is inconsistent with field observations. Furthermore, the volume of basalts within the study area is relatively low (Bosworth *et al.*, 2015) meaning it is unlikely that they were able to significantly modify fluid composition. The low concentrations of iron within the dolostone supports

this notion, since any contribution by magmatic fluids to dolomitizing fluids would most likely increase concentrations of iron in the resultant dolomite.

Controls on dolomitization

Preferential dolomitization of the debrite (R1) and turbidite (R2) facies suggests that there was a facies control on the occurrence of dolomitization, either because a) debrites and turbidites had higher permeabilities, and so focused fluid flux or b) there were differences in the mineralogy and texture of facies that controlled their dolomitization potential. The formation of discrete stratabound dolostone bodies has been recognised in many studies of fault-controlled dolomitization, and is often interpreted to reflect preferential dolomitization of highly permeable layers (Davies and Smith, 2006; Sharp *et al.*, 2010; Gomez-Rivas *et al.*, 2014; Corbella *et al.*, 2014). In this study, petrophysical measurements of remobilised limestone facies indicate that their present-day matrix permeability is only moderately higher than the undolomitized, interbedded, slope packstones and less than the basinal wackestone facies of the upper Thebes Formation. Since dolomitization took place within sediments that had reached maximum burial, the measured porosity and permeability of the limestones is considered to be largely representative of their matrix properties during dolomitization, although there was some subsequent porosity, and therefore permeability, loss as a result of telogenetic cementation.

Korneva *et al.*, (2017) describe the distribution of fractures within limestone and stratabound dolostone within the damage zone of, and at 2 km from, the HFF. During formation of the stratabound dolostone, fractures and faults would have been present at the tip of the HFF (Jackson *et al.*, 2005), but offset on the HFF was minimal and therefore the damage zone would have been narrow. Therefore, present-day fracture density at 2 km distance from the HFF might give some indication of likely fracture density during dolomitization. The highest fracture densities (narrowest spacing) recorded in Korneva *et al.*, (2017) are inslope packstones (S1), followed by matrix-supported conglomerates (R1) with the lowest density in turbidite grainstones (R2). It is possible, therefore, that the fracture network played an important role in the fluid flux away from the proto-HFF during dolomitization, perhaps facilitating dolomitization particularly in the R1 facies.

Nevertheless, sediment texture and composition may also have played a role. Since the debrites and grainstone turbidites (R1 and R2 respectively) are coarser grained than the slope packstones (S1) it seems unlikely that reactive surface area influenced the loci of dolomitization, although micritization of grains could have increased the reactive surface area of some grains. It is possible that the diverse range of shallow water grains within R1 and R2 facies, compared to S1 facies, facilitated dolomitization preferentially in remobilized beds. Since mineralogical stabilization would have occurred prior to dolomitization it is unclear how this control might have operated, but one possibility is that remnant microdolomite inclusions within former high magnesium calcite grains acted as seeds for dolomitization (e.g. Juerges *et al.*, 2016).

612 *Evidence for hydrothermal dolomitization*

613 Conceptual models of fault-controlled dolomitization typically interpret dolomitization to have occurred
 614 from hydrothermal, evolved, crustal fluids that are expelled at high pressure along faults, by seismic
 615 pumping, into the host rock (Davies and Smith, 2006). They form a number of characteristic features,
 616 including non-planar replacive dolomite, zebra dolomite and hydraulic breccias cemented by saddle
 617 dolomite, interpreted to reflect high pressure fluid expulsion and fluid effervescence (Davies and
 618 Smith, 2006; Gasparri *et al.*, 2006; Nader *et al.*, 2007; López-Horgue *et al.*, 2010; Sharp *et al.*, 2010;
 619 Dewit *et al.*, 2014). Machel and Lonnee (2002) criticised the misrepresentation of the term
 620 'hydrothermal' in many of these conceptual models and defined its use as strictly referring to
 621 dolostone bodies where dolomitizing fluids were $> 5^{\circ}\text{C}$ warmer than the host rock. On the HFF block,
 622 we interpret the stratabound dolostone bodies to be fault-controlled in the sense that dolomitizing
 623 fluids entered the Thebes Formation from the proto-HFF. Assuming that the base of the Thebes Fm.
 624 was at $\sim 700 - 850$ m burial depth during dolomitization, an elevated geothermal gradient of $48^{\circ}\text{C km}^{-1}$
 625 and an ambient seawater temperature of 30°C , the Thebes Formation would have been $< \sim 64 - 71^{\circ}\text{C}$.
 626 Since the temperature of dolomitizing fluids has been determined from clumped isotopes as $67-76^{\circ}\text{C}$,
 627 and from conventional isotopes as up to 83°C , then we can consider the stratabound dolostone bodies
 628 to be marginally to fully hydrothermal.

629 Nevertheless, many of the 'classic' features of fault-controlled hydrothermal dolomite are not
 630 observed. Zebra dolomite textures (Fig. 8B) are rare and we hypothesize that these features may
 631 have formed during the onset of transtension along the Aqaba-Levant transform, forming perhaps by
 632 pressure build-up beneath low permeability lenses (chert nodules in this case). They do not seem to
 633 be related to the main phase of stratabound dolomitization. Minor hydrobrecciation is seen within the
 634 damage zone of the HFF (Hirani *et al.*, in prep) but not in association with the stratabound dolostone.
 635 Saddle dolomite is conspicuously absent, despite fluid temperatures of $>60^{\circ}\text{C}$, suggesting that crystal
 636 growth rates were too slow and/or fluid saturations too low for rapid precipitation of dolomite with a
 637 saddle morphology.

638 Consequently, the results of this study indicate that fault-controlled, hydrothermal dolomitization
 639 cannot be interpreted on the basis of what are commonly perceived to be characteristic textural
 640 features. Indeed, in a subsurface environment, the textures encountered within the stratabound
 641 dolostone might result in a misinterpretation of their origin, and hence spatial distribution and length
 642 scales. Our conceptual model, based on the integration of field mapping, structural relationships,
 643 petrographical and geochemical data instead provides evidence for fault-controlled geothermal
 644 convection of seawater at elevated temperatures but without the high pressure expulsion, rupture and
 645 effervescence commonly associated with fault controlled dolomitization (*sensu* Davies and Smith,
 646 2006). Instead, the results suggest that geothermal convection, which is known to be an important
 647 control on the syn-depositional diagenetic modification of platform margins (e.g. Whitaker and Xiao,

2010; Jones and Xiao, 2006, 2013), can control diagenesis after burial in tectonically-active regions. Furthermore, it is possible for seawater to move up evolving, crustal-scale faults that have not undergone significant offset, or breached the surface, during the earliest phases of rifting. A significant advantage of this model is that it has fewer constraints with respect to fluid and Mg mass balance and so is able to more adequately explain the volume of in place dolostone than more commonly invoked models of fault-controlled dolomitization.

Overall, the relatively simple burial and uplift history of the Thebes Fm. provides an insight into a dolomitization process that might commonly develop within other syn-rift basins, but which may be obscured by subsequent diagenetic overprinting in basins that have a more complex, and long-lived, burial history.

Conclusions

The results of this study provide an insight into fluid flux and diagenetic processes during rift initiation.

- Stratabound dolostone bodies on the HFF block formed almost exclusively within debrites and grainstone turbidite facies of the lower Thebes Fm. from heated, slightly evaporated Oligo-Miocene seawater.
- Faults appear to have provided permeable pathways that connected seawater with the deep, Nubian aquifer, enabling development of convective circulation driven by geothermal heating. These fluids ascended the proto-HFF, facilitated by heat generated during initial rifting. The resulting buoyant fluids utilised the fault as a conduit, escaping upwards and then flowing laterally into the lower Thebes Fm. Evidence for this is only exposed in the footwall of the HFF, but conceptual and flow models would support a similar distribution of stratabound dolostone in the hanging wall.
- The main control on the formation of stratabound dolostone could be the depth of the tip of the HFF, and the higher permeability of the Thebes Fm. compared to the bounding formations. Within the Thebes Fm., dolomitization may have been influenced by fracture permeability and potentially the chemical reactivity of the precursor dolomitized facies.
- Dolomitization has been constrained by field relationships and the structural evolution of the platform to a ~10 Ma period during the Oligo-Miocene, after rift initiation and prior to the rift climax.
- The conceptual model of dolomitization from convecting seawater presented in this paper might be more common than recognized by the current literature. It has been observed in a few case studies from other basins, and it may well be a common process during the earliest stages of rifting, leading to selective dolomitization of pre-rift and possibly syn-rift carbonate platforms.

Acknowledgements

Stable isotope analysis was conducted under NERC award IP-1357-1112 at the NERC Isotope Geosciences Facility in East Kilbride. Strontium isotope analysis was conducted at University of Brest and Dr Stefan LaLonde is thanked for his help. This project was funded via ITF project 3310PSD by BG-Group, Saudi Aramco, Statoil and Total. Falcon of the Desert, Anja Eker, Michael Laukemann, Thomas Seers, Richard Newport and David Hodgetts are gratefully acknowledged for field support. We would like to thank David Budd, Miles Frazer and Gareth Jones for thoughtful and detailed reviews of this, and an earlier version of this manuscript, which has helped to significantly improve the quality of this paper.

References

- Abul-Nasr, R. A., 1987.** Biostratigraphy and facies analysis of some Eocene exposures, west central Sinai, Egypt, University of South Carolina, U.S.A.
- Abuseda, H., Kassab, M.A., LaLa, A.M and El Sayed., N.A., 2015.** Integrated petrographical and petrophysical studies of some Eocene carbonate rocks, southwest Sinai, Egypt. *Egyptian Journal of Petroleum*, **24**, 213– 230
- Alsharhan, A. S., and Salah, M. G. 1995.** Geology and hydrocarbon habitat in rift setting: northern and central Gulf of Suez, Egypt. *Bulletin of Canadian Petroleum Geology*. **43**,156-176.
- Armstrong, B., 1997.** The temporal and spacial evolution of clastic syn-tectonic sedimentation on and adjacent to a developing relay ramp: an example from the Suez Rift. [Ph.D. thesis]: *University of Edinburgh*, 134 pp.
- Banner, J. L., Hanson, G., and Meyers, W., 1988.** Rare earth element and Nd isotopic variations in regionally extensive dolomites from the Burlington-Keokuk Formation (Mississippian): Implications for REE mobility during carbonate diagenesis. *Journal of Sedimentary Research*. **58**, 415-432.
- Bau, M., and Dulski, P., 1996** Distribution of yttrium and rare-earth elements in the Penge and Kuruman iron-formations, Transvaal Supergroup, South Africa. *Precambrian Research*. **79**, 37-55.
- Bayon, G., Barrat, J. A., Etoubleau, J., Benoit, M., Bollinger, C., and Révillon, S., 2009** Determination of rare earth elements, Sc, Y, Zr, Ba, Hf and Th in geological samples by ICP-MS after Tm addition and alkaline fusion. *Geostandards and Geoanalytical Research*. **33**, 51-62.
- Boni, M., Iannace, A., Bechstädt, T., and Gasparrini, M., 2000.** Hydrothermal dolomites in SW Sardinia (Italy) and Cantabria (NW Spain): evidence for late-to post-Variscan widespread fluid-flow events. *Journal of Geochemical Exploration*. **69**, 225-228.
- Bosworth, W., Huchon, P., and McClay, K., 2005** The Red Sea and Gulf of Aden basins. *Journal of African Earth Sciences*. **43**, 334-378.
- Bosworth, W., Stockli, D and Helgeson, D., 2015.** Integrated outcrop, 3D seismic and geochronological interpretation of Red Sea dike-related deformation in the Western Desert, Egypt- the role of the 23Ma Cairo 'mini-plume'. *Journal of African Earth sciences*, **109**, 107-119
- Boulos, F., 1990.** Some aspects of the geophysical regime of Egypt in relation to heat flow, groundwater and microearthquakes. In: *The Geology of Egypt (Ed. R. Said)*. 61 - 89.

- 722 **Brand, U. and Veizer, J., 1980.** Chemical diagenesis of a multicomponent carbonate system; 1,
723 Trace elements. *Journal of sedimentary research*. **50**,1219-1236.
- 724 **Brennan, S., Lowenstein T., and Cendón. D., 2013.** The major-ion composition of Cenozoic
725 seawater: The past 36 million years from fluid inclusions in marine halite. *American Journal of*
726 *Science*. **313**, 713-775.
- 727 **Cervato, C., 1990.** Hydrothermal dolomitization of Jurassic-Cretaceous limestones in the southern
728 Alps (Italy): Relation to tectonics and volcanism. *Geology*. **18**, (5) 458-461.
- 729 **Corbella, M., Gomez-Rivas, E., Martín-Martín, J., Stafford, S., Teixell, A., Grier, A., Travé, A.,**
730 **Cardellach, E., and Salas, R. 2014.** Insights to controls on dolomitization by means of reactive
731 transport models applied to the Benicàssim case study (Maestrat Basin, eastern Spain). *Petroleum*
732 *Geoscience*. **20**, 41-54.
- 733 **Dale, A., Mozley, P. S., Smalley, P. C., & Muggeridge, A. H., 2014.** Time-capsule concretions:
734 Unlocking burial diagenetic processes in the Mancos Shale using carbonate clumped isotopes. *Earth*
735 *and Planetary Science Letters*, **394(C)**, 30–37. <http://doi.org/10.1016/j.epsl.2014.03.004>
- 736 **Davies, G. R., and Smith, L. B. , 2006.** Structurally controlled hydrothermal dolomite reservoir facies:
737 An overview. *American Association of Petroleum Geologists Bulletin*. **90**, 1641-1690.
- 738 **Dennis, K. J., Affek, H. P., Passey, B. H., Schrag, D. P., & Eiler, J. M., 2011.** Defining an absolute
739 reference frame for “clumped” isotope studies of CO₂. *Geochimica et Cosmochimica Acta*, **75**, 7117–
740 7131. <http://doi.org/10.1016/j.gca.2011.09.025>
- 741 **Dewit, J., Foubert, A., El Desouky, H., Muchez, P., Hunt, D., Vanhaecke, F., and Swennen, R.,**
742 **2014.** Characteristics, genesis and parameters controlling the development of a large stratabound
743 HTD body at Matienzo (Ramales Platform, Basque-Cantabrian Basin, northern Spain). *Marine and*
744 *Petroleum Geology*. **55**, 6-25.
- 745 **Dickson, J. A. D., 1966.** Carbonate identification and genesis as revealed by staining. *Journal of*
746 *Sedimentary Research*. **36**, 491-505.
- 747 **Dunham, R. J., 1962.** Classification of carbonate rocks according to depositional texture. *American*
748 *Association of Petroleum Geologists Memoirs*. **1**, 108-121.
- 749 **Eppelbaum, L., Kutasov, I and Pilchin. A, 2014.** Thermal properties of rocks and density of fluids.
750 *Applied Geothermics*, 99–149

- 751 **Gasparrini, M., Bechstädt, T., and Boni, M., 2006.** Massive hydrothermal dolomites in the
 752 southwestern Cantabrian Zone (Spain) and their relation to the Late Variscan evolution. *Marine and*
 753 *Petroleum Geology*. **23**, 543-568.
- 754 **Gawthorpe, R. L., and Hurst, J. M., 1993.** Transfer zones in extensional basins: their structural style
 755 and influence on drainage development and stratigraphy. *Journal of the Geological Society*. **150**,
 756 1137-1152.
- 757 **Gawthorpe, R. L., Jackson, C. A. L., Young, M. J., Sharp, I. R., Moustafa, A. R., and Leppard, C.**
 758 **W., 2003.** Normal fault growth, displacement localisation and the evolution of normal fault populations:
 759 the Hammam Faraun fault block, Suez rift, Egypt. *Journal of Structural Geology*. **25**, 883-895.
- 760 **Giles, M., 1987.** Mass transfer and problems of secondary porosity creation in deeply buried
 761 hydrocarbon reservoirs, *Marine and Petroleum Geology*, **4**, 188-204
- 762 **Gillhaus, A., Richter, D. K., Götze, T., and Neuser, R. D., 2010.** From tabular to rhombohedral
 763 dolomite crystals in Zechstein 2 dolostones from Scharzfeld (SW Harz/Germany): A case study with
 764 combined CL and EBSD investigations. *Sedimentary Geology*. **228**, 284-291.
- 765 **Gomez-Rivas, E., Corbella, M., Martín-Martín, J.D., Stafford, S.L., Teixell, A., Bons, P.D., Grier, A.**
 766 **A. and Cardellach, E., 2014** Reactivity of dolomitizing fluids and Mg source evaluation of fault-
 767 controlled dolomitization at the Benicassim outcrop analogue (Maestrat Basin, E Spain). *Marine and*
 768 *Petroleum Geology*. **55**, 26-42.
- 769 **Gregg, J., 2004** Basin fluid flow, base-metal sulphide mineralization and the development of dolomite
 770 petroleum reservoirs. In: *The Geometry and Petrogenesis of Dolomite Hydrocarbon Reservoirs* (Ed. C.
 771 Braithwaite, G. Rizzi and G. Darke). Geological Society London Special Publications, **235**, 157-175
- 772 **Guo, W., Mosenfelder, J. L., Goddard III, W. A., and Eiler, J. M., 2009.** Isotopic fractionations
 773 associated with phosphoric acid digestion of carbonate minerals: insights from first-principles
 774 theoretical modeling and clumped isotope measurements. *Geochimica et Cosmochimica Acta*. **73**,
 775 7203-7225.
- 776 **Haley, B. A., Klinkhammer, G. P., and McManus, J. 2004.** Rare earth elements in pore waters of
 777 marine sediments. *Geochimica et Cosmochimica Acta*. **68**, 1265-1279.
- 778 **Hassanain, I. M., Abdou, M. I., & Abu Seda, H. H., 2012.** Petrographical and Petrophysical Studies
 779 of Some Upper Cretaceous Rocks, Southwest Sinai, Egypt. *Petroleum Science and Technology*. **30**,
 780 64-73.

- 781 **Hirani, J., 2014.** Diagenetic evaluation of fault/fracture related dolomitization, Cretaceous-Eocene,
 782 Hammam Faraun Fault Block, Gulf of Suez. [Ph.D. thesis]: *University of Manchester*, 295 pp.
- 783 **Hollis, C., Bastesen, B., Boyce, A., Corlett, H., Gawthorpe, R., Hirani, J., Rotevatn, A., and**
 784 **Whitaker, F. 2017** Fault-controlled dolomitization within rift basins. *Geology*. **45**.
- 785 **Höntzsch, S., Scheibner, C., Kuss, J., Marzouk, A.M., and Rasser, M.W., 2011.** Tectonically driven
 786 carbonate ramp evolution at the southern Tethyan shelf: the Lower Eocene succession of the Galala
 787 Mountains, Egypt. *Facies*, **57**, 51-72.
 788 **Horita, J. (2014).** Oxygen and carbon isotope fractionation in the
 789 system dolomite-water-CO₂ to elevated temperatures. *Geochimica et Cosmochimica Acta*, **129**, 111–
 124. <http://doi.org/10.1016/j.gca.2013.12.027>
- 790 **Horwitz, E. P., and Bloomquist, C. A. A., 1975.** Chemical separations for super-heavy element
 791 searches in irradiated uranium targets. *Journal of Inorganic and Nuclear Chemistry*. **37**, 425-434.
- 792 **Huntington, K. W., Eiler, J. M., Affek, H. P., Guo, W., Bonifacie, M., Yeung, L. Y., 2009.** Methods
 793 and limitations of “clumped” CO₂ isotope (Delta47) analysis by gas-source isotope ratio mass
 794 spectrometry. *Journal of Mass Spectrometry*, **44**, 1318–1329. <http://doi.org/10.1002/jms.1614>
- 795 **Jackson, C. A. L., Gawthorpe, R. L., Carr, I. D., and Sharp, I. R., 2005.** Normal faulting as a control
 796 on the stratigraphic development of shallow marine syn-rift sequences: the Nukhul and Lower Rudeis
 797 Formations, Hammam Faraun fault block, Suez Rift, Egypt. *Sedimentology*. **52**, 313-338.
- 798 **Jackson, C. A. L., Gawthorpe, R. L., Leppard, C. W., and Sharp, I. R., 2006.** Rift-initiation
 799 development of normal fault blocks: insights from the Hammam Faraun fault block, Suez Rift, Egypt.
 800 *Journal of the Geological Society*. **163**, 165-183.
- 801 **Jarrige, J.-J., d'Estevou, P. O., Buroillet, P. F., Montenat, C., Prat, P., Richert, J.-P., and Thiriet,**
 802 **J.-P., 1990.** The multistage tectonic evolution of the Gulf of Suez and northern Red Sea continental rift
 803 from field observations. *Tectonics*, **9**, 441-465.
- 804 **John, C. M., & Bowen, D., 2016.** Community software for challenging isotope analysis: First
 805 applications of "Easotope" to clumped isotopes. *Rapid Communications in Mass Spectrometry*, **30**,
 806 2285–2300. <http://doi.org/10.1002/rcm.7720>
- 807 **Jones, C. E., Jenkyns, H. C., Coe, A. L., and Stephen, H. P., 1994.** Strontium isotopic variations in
 808 Jurassic and Cretaceous seawater. *Geochimica et Cosmochimica Acta*. **58**, 3061-3074.
- 809 **Jones, G and Xiao, Y, 2006** Geothermal convection in the Tengiz carbonate platform, Kazakhstan:
 810 Reactive transport models of diagenesis and reservoir quality. *AAPG Bulletin*, **90**, 1251-1272

- 811 **Jones, G and Xiao, Y, 2013.** Geothermal convection in South Atlantic subsalt lacustrine carbonates:
 812 Developing diagenesis and reservoir quality predictive concepts with reactive transport models.
 813 AAPG Bulletin, 97, 1249-1271
- 814 **Juerges, A., Hollis, C., Marshall, J and Crowley, S., 2016,** The control of basin evolution on
 815 patterns of sedimentation and diagenesis: an example from the Mississippian Great Orme, North
 816 Wales. *Journal of the Geological Society, London.* doi:10.1144/jgs2014-149
- 817 **Khalil, S. M., and McClay, K. R., 2001.** Tectonic evolution of the NW Red Sea–Gulf of Suez rift
 818 system. *Non-Volcanic Rifting of Continental Margins: A Comparison from Land and Sea.* **187**, 453-
 819 473.
- 820 **Kluge, T., John, C. M., Jourdan, A.-L., Davis, S., & Crawshaw, J., 2015.** Laboratory calibration of
 821 the calcium carbonate clumped isotope thermometer in the 25–250°C temperature range. *Geochimica*
 822 *Et Cosmochimica Acta*, **157**, 213–227. <http://doi.org/10.1016/j.gca.2015.02.028>
- 823 **Knott, S. D., Beach, A., Welbon, A. I., and Brockbank, P. J., 1995.** Basin inversion in the Gulf of
 824 Suez: implications for exploration and development in failed rifts. *Geological Society, London, Special*
 825 *Publications.* **88**, 59-81.
- 826 **Koepnick, R., Burke, W., Denison, R., Hetherington, E., Nelson, H., Otto, J., and Waite, L., 1985**
 827 Construction of the seawater $^{87}\text{Sr}/^{86}\text{Sr}$ curve for the Cenozoic and Cretaceous: Supporting data.
 828 *Chemical Geology: Isotope Geoscience section.* **58**, 55-81.
- 829 **Korneva, I., Bastesen, E., Corlett, H., Eker, A., Hirani, J., Hollis, C., Gawthorpe, R.L., Rotevatn,**
 830 **A. and Taylor, R. 2017.** The effects of dolomitization on petrophysical properties and fracture
 831 distribution within rift-related carbonates (Hammam Faraun Fault Block, Suez Rift, Egypt). *Journal of*
 832 *Structural Geology.*
- 833 **Krumgalz, B.S., 2001** Application of the Pitzer ion interaction model to natural hypersaline brines.
 834 *Journal of Molecular Liquids*, **91**, 3-19.
- 835 **Lashin. A., 2013.** A preliminary study on the potential of the geothermal resources around the Gulf of
 836 Suez, Egypt. *Arabian Journal of Geosciences*, **6**, 2807–2828
- 837 **Leppard, C. W., and Gawthorpe, R. L., 2006** Sedimentology of rift climax deep water systems; Lower
 838 Rudeis Formation, Hammam Faraun Fault Block, Suez Rift, Egypt. *Sedimentary Geology.* **191**, 67-87.
- 839 **Ligi M., Bonati, E, Cuffano, M and Brunelli, D., 2013.** Post Mesozoic Rapid Increase of Seawater
 840 Mg/Ca due to Enhanced Mantle-Seawater Interaction. *Scientific Reports*, 3:2752, doi:
 841 10.1038/srep02752

- 842 **Lonnee, J., and Machel, H. G., 2006.** Pervasive dolomitization with subsequent hydrothermal
 843 alteration in the Clarke Lake gas field, Middle Devonian Slave Point Formation, British Columbia,
 844 Canada. *American Association of Petroleum Geologists Bulletin*. **90**, 1739-1761.
- 845 **López-Horgue, M. A., Iriarte, E., Schröder, S., Fernández-Mendiola, P. A., Caline, B., 2009.** An
 846 example on the tectonic origin of zebra dolomites: the San Martin beach outcrop (Santona, North
 847 Spain). *Geogaceta*, **47**, 85-88
- 848 **López-Horgue, M. A., Iriarte, E., Schröder, S., Fernández-Mendiola, P. A., Caline, B., Corneyllie,**
 849 **H., Frémont, J., Sudrie, M., and Zerti, S., 2010.** Structurally controlled hydrothermal dolomites in
 850 Albian carbonates of the Asón valley, Basque Cantabrian Basin, Northern Spain. *Marine and*
 851 *Petroleum Geology*, **27**, 1069-1092.
- 852 **Lumsden, D. N., 1979.** Discrepancy between thin-section and X-ray estimates of dolomite in
 853 limestone. *Journal of Sedimentary Research*, **49**, 429-435.
- 854 **Machel, H and Lonnee, J., 2002** Hydrothermal dolomite- a product of poor definition and imagination.
 855 *Sedimentary Geology*, **152**, 163-171
- 856 **Machel, H. G., and Burton, E. A., 1991.** Factors governing cathodoluminescence in calcite and
 857 dolomite, and their implications for studies of carbonate diagenesis. In *Luminescence Microscopy and*
 858 *Spectroscopy: Qualitative and Quantitative Applications*: Special Publications of SEPM.
- 859 **Matthews, A., and Katz, A. 1977.** Oxygen isotope fractionation during the dolomitization of calcium
 860 carbonate. *Geochimica et Cosmochimica Acta*. **41**, 1431–1438.
- 861 **McCrea, J. M., 1950.** On the isotopic chemistry of carbonates and a paleotemperature scale. *The*
 862 *Journal of Chemical Physics*, **18**, 849.
- 863 **Melim, L., Westphal, H., Swart, P., Eberli, G. and Munnecke, A., 2002.** Questioning carbonate
 864 diagenetic paradigms: evidence from the Neogene of the Bahamas. *Marine Geology*, **185**, 27-53
- 865 **Montenat, C., Ott d'Estevou, P., and Purser, B. Burollet, P-F., Jarrige, J.-J., Orsazag-Sperber, F.,**
 866 **Philobbos, E., Plaziat, J.-C., Prat, P., Richert, J.-P., Roussel, N. and Thiriet, J.-P., 1988.** Tectonic
 867 and sedimentary evolution of the Gulf of Suez and the northwestern Red Sea. *Tectonophysics*, **153**,
 868 161-177.
- 869 **Mousa, A. S., El-Hariri, T. Y., & Assy, E. M. A., 2011.** Sedimentological and petrophysical
 870 characteristics of Raha Formation at Wadi Tubia, Northern Gulf of Aqaba, Sinai, Egypt. *Egyptian*
 871 *Journal of Petroleum*. **20**, 79-87.

- 872 **Moustafa, A. R., 1996.** Internal structure and deformation of an accommodation zone in the northern
873 part of the Suez rift. *Journal of Structural Geology*. **18**, 93-107.
- 874 **Moustafa, A.R., 2003,** Explanatory notes for the geologic maps of the eastern side of the Suez Rift
875 (western Sinai Peninsula): *American Association of Petroleum Geologists Datapages GIS Series 34*.
- 876 **Moustafa, A. R., and Abdeen, M. M., 1992.** Structural setting of the Hammam Faraun block, eastern
877 side of the Suez rift. *Journal of the University of Kuwait (Science)*, **19**, 291-291.
- 878 **Murray, S. and Swart, P., 2017.** Evaluating Formation Fluid Models and Calibrations Using Clumped
879 Isotope Paleothermometry on Bahamian Dolomites. *Geochimica et Cosmochimica Acta*, In press
- 880 **Nabawy, B, Geraud, Y., Rochette, P and Bur, N, 2009** Pore throat characterization in highly porous
881 and permeable sandstones. *American Association of Petroleum Geologists Bulletin*. **93**, 719-739.
- 882 **Nader, F. H., Swennen, R., Ellam, R. M., and Immenhauser, A., 2007.** Field geometry, petrography
883 and geochemistry of a dolomitization front (Late Jurassic, central Lebanon). *Sedimentology*. **54**, 1093-
884 1120.
- 885 **Nance, W. B., and Taylor, S. R., 1976** Rare earth element patterns and crustal evolution—I.
886 Australian post-Archean sedimentary rocks. *Geochimica et Cosmochimica Acta*, **40**, 1539-1551.
- 887 **Nothdurft, L. D., Webb, G. E., and Kamber, B. S., 2004.** Rare earth element geochemistry of Late
888 Devonian reefal carbonates, Canning Basin, Western Australia: confirmation of a seawater REE proxy
889 in ancient limestones. *Geochimica et Cosmochimica Acta*. **68**, 263-283. **Passey, B. H., and Henkes,**
890 **G. A., 2012.** Carbonate clumped isotope bond reordering and geospeedometry. *Earth and Planetary*
891 *Science Letters*. **351**, 223-236.
- 892 **Parkhurst, D.L. and Appelo, C.A.J., 2013** Description of input and examples for PHREEQC version
893 3. A computer program for speciation, batch-reaction, one-dimensional transport, and inverse
894 geochemical calculations: U.S. Geological Survey Techniques and Methods, book 6, chap. A43, 497
- 895 **Patton, T. L., Moustafa, A. R., Nelson, R. A., and Abdine, S. A., 1994.** Tectonic evolution and
896 structural setting of the Suez Rift. *American Association of Petroleum Geologists Memoirs*. **59**, 9-55.
- 897 **Pearson, P. N., Ditchfield, P. W., Singano, J., Harcourt-Brown, K. G., Nicholas, C. J., Olsson, R.**
898 **K., Shackleton, N. J., and Hall, M. A., 2001.** Warm tropical sea surface temperatures in the Late
899 Cretaceous and Eocene epochs. *Nature*. **413**, 481-487.
- 900 **Pearson, M and Garven, G., 1992** Hydrologic constraints on petroleum generation within continental
901 rift basins: theory and application to the Rhine Graben. *AAPG Bulletin*, **76**, 468-488

- 902 **Plummer, L.N., Parkhurst, D.L., Fleming, G.W. and Dunkle, S.A., 1988** A Computer Program
 903 Incorporating Pitzer's Equations for Calculation of Geochemical Reactions in Brines. U.S. Geological
 904 Survey Water-Resources Investigations Report 88-4153.
- 905 **Pomeyrol, R., 1968.** Nubian sandstone. *American Association of Petroleum Geologists Bulletin*, **52**,
 906 589-600.
- 907 **Prokoph, A., Shields, G.A. and Veizer, J., 2008.** Compilation and time-series analysis of a marine
 908 carbonate $\delta^{18}\text{O}$, $\delta^{13}\text{C}$, $^{87}\text{Sr}/^{86}\text{Sr}$ and $\delta^{34}\text{S}$ database through Earth history. *Earth-Science Reviews*, **87**
 909 113-133.
- 910 **Pruess, K. 1991.** TOUGH2: A general-purpose numerical simulator for multiphase fluid and heat flow.
 911 *NASA STI/Recon Technical Report N 92: 14316.*
- 912 **Refaat, A., and Imam, M., 1999.** The Tayiba Red Beds: transitional marine-continental deposits in the
 913 precursor Suez rift, Sinai, Egypt. *Journal of African Earth Sciences*, **28**, 487-506.
- 914 **Reilly, T. J., Miller, K. G., and Feigenson, M. D., 2002.** Latest Eocene-earliest Miocene Sr isotopic
 915 reference section, Site 522, eastern South Atlantic. *Paleoceanography*, **17**, 18-11.
- 916 **Robson, D.A., 1971.** The structure of the Gulf of Suez (Clysmic) rift, with special reference to the
 917 eastern side. *Journal of the Geological Society*, **127**, 247-271.
- 918 **Rosenbaum, J., and Sheppard, S. M. F., 1986.** An isotopic study of siderites, dolomites and
 919 ankerites at high temperatures. *Geochimica et Cosmochimica Acta*, **50**, 1147-1150.
- 920 **Rusticelli, A., Iannace, A., Tondi, E., di Celma, C., Cilona, A., Giorgioni, M., Parente, M.,**
 921 **Girundo, M and Invernizzi, C., 2016.** Fault-controlled dolomite bodies as palaeotectonic indicators
 922 and geofluid reservoirs: new insights from Gargano Promontory outcrops. *Sedimentology*
- 923 **Salah M. and Al-Sharhan, A., 1998.** The Precambrian basement: a major reservoir in the rifted basin,
 924 Gulf of Suez. *Journal of Petroleum Science and Engineering*, **19**, 201–222
- 925 **Sefelnasr, A. M., 2007.** Development of groundwater flow model for water resources management in
 926 the development areas of the western desert, Egypt. *DSc, Martin Luther University, Germany.*
- 927 **Sharp, I., Gillespie, P., Morsalnezhad, D., Taberner, C., Karpuz, R., Vergés, J., Horbury, A.,**
 928 **Pickard, N., Garland, J., and Hunt, D., 2010.** Stratigraphic architecture and fracture-controlled
 929 dolomitization of the Cretaceous Khami and Bangestan groups: an outcrop case study, Zagros
 930 Mountains, Iran. *Geological Society, London, Special Publications*. **329**, 343-396.

- 931 **Sharp, I. R., Gawthorpe, R. L., Underhill, J. R., and Gupta, S., 2000.** Fault-propagation folding in
 932 extensional settings: Examples of structural style and synrift sedimentary response from the Suez rift,
 933 Sinai, Egypt. *Geological Society of America Bulletin*. **112**, 1877-1899.
- 934 **Sibley, D. F., and Gregg, J. M., 1987.** Classification of dolomite rock textures. *Journal of Sedimentary*
 935 *Research*. **57**, 967-975.
- 936 **Steckler, M. S., Berthelot, F., Lyberis, N., and Le Pichon, X., 1988.** Subsidence in the Gulf of Suez:
 937 implications for rifting and plate kinematics. *Tectonophysics*. **153**, 249-270.
- 938 **Sturchio, T., Arehart, G, Sultan, M., Sano, Y, AboKamer, Y and Sayed, M. ,1996.** Composition and
 939 origin of thermal waters in the Gulf of Suez area, Egypt. *Applied Geochemistry*, **11**, 471-479.
- 940 **Vahrenkamp, V and Swart, P., 1990** New distribution coefficient for the incorporation of strontium into
 941 dolomite and its implications for the formation of ancient dolomites. *Geology*, **18**, 387-391
- 942 **Wang, Z., Schauble, E. A., & Eiler, J. M. ,2004.** Equilibrium thermodynamics of multiply substituted
 943 isotopologues of molecular gases. *Geochimica et Cosmochimica Acta*, **68**, 4779–4797.
 944 <http://doi.org/10.1016/j.gca.2004.05.039>
- 945 **Webb, G. E., and Kamber, B. S., 2000.** Rare earth elements in Holocene reefal microbialites: a new
 946 shallow seawater proxy. *Geochimica et Cosmochimica Acta*. **64**, 1557-1565.
- 947 **Weissbrod, T., and Nachmias, J. 1986** Stratigraphic significance of heavy minerals in the late
 948 Precambrian-Mesozoic clastic sequence ("Nubian Sandstone") in the near east. *Sedimentary*
 949 *Geology*, **47**, 263-291.
- 950 **Wierzbicki, R, Dravis, J, Al-Aasm, I and Harland, N., 2006** Burial dolomitization and dissolution of
 951 Upper Jurassic Abenaki platform carbonates, Deep Panuke reservoir, Nova Scotia, Canada. *AAPG*
 952 *Bulletin*, **90**, 1843-1861
- 953 **Whitaker, F. F., and Xiao, Y., 2010.** Reactive transport modeling of early burial dolomitization of
 954 carbonate platforms by geothermal convection. *American Association of Petroleum Geologists*
 955 *Bulletin*, **94**, 889-917.
- 956 **Wilson, M, Evans, M., Oxtoby, N, Satria Nas, D., Donnelly, T and Thirlwall, M. 2007** Reservoir
 957 quality, textural evolution and origin of fault-associated dolomites. *AAPG Bulletin*, **91**, 1247-1272
- 958 **Woodman, P., 2009.** Controls on rift-climax sedimentation: impact of sediment sources, sea-level
 959 change and tectonics. Examples from the Gulf of Suez Rift, Egypt. [Ph.D. thesis]: University of
 960 Manchester, 401 pp.

- 961 **Wyndham, T., McCulloch, M., Fallon, S., and Alibert, C., 2004.** High-resolution coral records of rare
 962 earth elements in coastal seawater: biogeochemical cycling and a new environmental proxy.
 963 *Geochimica et Cosmochimica Acta*. **68**, 2067-2080.
- 964 **Younes, A. I., and McClay, K., 2002.** Development of accommodation zones in the Gulf of Suez-Red
 965 Sea rift, Egypt. *American Association of Petroleum Geologists Bulletin*. **86**, 1003-1026.
- 966 **Zaher, M. A., Saibi, H., Nishijima, J., Fujimitsu, Y., Mesbah, H., and Ehara, S., 2011** Exploration
 967 and assessment of the geothermal resources in the Hammam Faraun hot spring, Sinai Peninsula,
 968 Egypt. *Journal of Asian Earth Sciences*. **45**, 256-267.
- 969 **Zalat, A., Zaid, S., Gadallah, M. and Abdel-Aziz, Z., 2012** Sandstones reservoir quality of the Matulla
 970 Formation, Gulf of Suez, Egypt. *Australian Journal of Basic and Applied Sciences*, **6**, 511–529.
- 971 **Zheng, Y.F. and Hoefs, J., 1993.** Carbon and oxygen isotopic covariations in hydrothermal
 972 calcites. *Mineralium Deposita*. **28**, 79-89.

Figure Captions

Figure 1 (A) Map showing the major structural elements of the Gulf of Suez and distribution of pre-rift and syn-rift sediments along the western Sinai coast (adapted from Younes and McClay, 2002 and Khalil and McClay, 2002). (B) Composite stratigraphic section of the Hammam Faraun Fault block (adapted from Sharp et al., 2000 and Jackson et al., 2006). This study focuses on the pre-rift Thebes Formation

Figure 2 (A) Geological map of the study area within the Hammam Faraun Fault block (modified from Moustafa and Abdeen, 1992 and Moustafa, 2003). The Hammam Faraun Fault parallels the present day coastline, with the Gebel Fault intersecting through the study area. (B) Stratigraphic column of the Thebes Fm. in the study area. The stratabound dolostone bodies are stratigraphically controlled, occurring primarily within the lower Thebes Fm.

Figure 3 Oblique view of study area (direction of view annotated in Fig. 2a) showing the distribution and extent of stratabound dolostone bodies relative to the Hammam Faraun Fault and the Gebel Fault, superimposed onto a Google Earth image. The origin of the massive dolostone bodies in the study area are further discussed in Hollis *et al.* (2017).

Figure 4. (A) and (B) Sharp, planar contacts (arrows) between dark brown dolostone bodies and adjacent cream coloured host limestone beds

Figure 5. Photomicrographs showing the petrographic features of the precursor limestones in plane polarised light. **(A)** Recrystallised grainflow grainstone, with both matrix and allochems replaced by micro spar calcite. **(B)** Unaltered basinal wackestones, with microporous mud matrix and mosaic calcite within the internal structure of the pelagic foraminifera.

Figure 6. (A) PAAS normalised REE concentrations comparing the REE patterns for averaged unaltered and recrystallised limestones to the stratabound dolostones. Positive La and negative Ce anomalies are present in each case, however a flattening in the HREE's is observed within the dolomite samples, as seen within the recrystallised limestone samples. A notable decrease in the total REE concentration of the stratabound dolomites is observed relative to the host limestones. (B) PAAS normalised $(Pr/Pr^*)_{SN}$ versus $(Ce/Ce^*)_{SN}$ cerium anomaly plot (Webb and Kamber, 2000) showing that all samples cluster tightly in the field of negative Ce and positive La anomalies. (C) Sr concentration relative to dolomite stoichiometry, illustrating an increase in Sr with increasing mol% $CaCO_3$, as per Vahrenkamp and Swart (1990), shown by dotted line.

Fig. 7. (A) Stable isotope ($\delta^{18}O$ vs. $\delta^{13}C$) plot for unaltered limestones, recrystallised limestones, and stratabound dolostone samples. The whole rock isotopic composition for the unaltered limestones lie within the range that is expected for deposition from Eocene seawater (Pearson et al., 2001). In

comparison, the recrystallised limestone and dolostone samples exhibit lower $\delta^{18}\text{O}$ values ranging between -3.62‰VPDB and -8.04‰VPDB . (B) Temperature of dolomitizing fluids versus $\delta^{18}\text{O}_{\text{seawater}}$ plot for the stratabound dolostone bodies. This plot is constructed using the Matthews and Katz (1977) fractionation equation and can be used to determine the minimum and maximum temperature of dolomitizing fluids using the heaviest and lightest $\delta^{18}\text{O}_{\text{dolomite}}$ values. Assuming a $\delta^{18}\text{O}_{\text{seawater}}$ of $+1\text{‰}$ to 0‰ (Veizer and Prokoph, 2015), a minimum fluid temperature of 40°C and a maximum fluid temperature of 78°C would be expected. (C) Clumped isotope temperatures (y-axis, $^{\circ}\text{C}$) versus calculated $\delta^{18}\text{O}_{\text{water}}$ (x-axis, ‰ VSMOW) for three dolomite samples in this study. The shaded area represents the 68% confidence interval for each sample. Dashed lines represent the temperature range at which all three samples overlap at the 68% confidence interval ($69\text{--}78^{\circ}\text{C}$); this corresponds to a calculated fluid composition of approximately 2.5‰ VSMOW .

Figure 8 Macroscopic features of the stratabound dolostone bodies in the field. (A) Dark brown clast and grey matrix fabric within the stratabound bodies, both composed of dolomite. (B) Randomly orientated zebra dolomite-like fabrics, with elongated vuggy porosity. (C) Dogtooth calcite cement partially occluding vuggy porosity within zebra fabric. (D) Large botryoidal calcite cement partially cementing vuggy porosity. (E) Mouldic pores after clasts (arrow) of variable size. (F) Stratabound dolostone body lacking the presence of clast, clast pores or large vuggy pores, suggesting dolomitization of grainstone turbidite (R2) facies.

Figure 9. Photomicrographs of various dolomite textures, in plane polarised light (PPL, left) and cathodoluminescence (CL, right). (A) Planar-s dolomite in PPL and (B) in CL, showing mottled bright red and orange luminescent dolomite cores, overlain by a thick dull green luminescent zone and a thin bright red luminescent outer zone. (C) Matrix with non-planar dolomite texture in PPL, (D) corresponding CL image of non-planar dolomite showing mottled bright red and orange luminescence with limited zonation. (E) Non-planar dolomite in PPL and (F) corresponding CL image with mottled red and orange luminescence with zonation difficult to identify.

Figure 10. (A) Photomicrograph in PPL of cloudy core clear rim planar-s dolomite texture within a clast, and non-planar dedolomitised matrix. The clast and matrix are separated by a corrosion rim (arrow), (B) corresponding CL image with clast exhibiting mottled bright red and orange luminescent dolomite crystals. The matrix primarily exhibits non-luminescence, with minor patches of bright red and orange luminescence.

Figure 11. Strontium isotopic ratios relative to the seawater strontium curve (Koepnick et al., 1985) and tectonic events of the Hammam Faraun Fault block. The time of formation of the Thebes Fm. is also highlighted. The unaltered and recrystallised limestones correspond to Late Eocene to Early Oligocene seawater. The stratabound dolostone bodies correspond to middle Oligocene to Early Miocene seawater strontium ratios, and the late pre-rift to rift initiation tectonic phase.

Figure 12. Burial history curve for the base Thebes Fm. in the hangingwall and footwall of the Hammam Faraun Fault block. Knowledge of the pre-rift and syn-rift sediment deposition is utilised to construct the burial history for both the hangingwall and footwall succession (Steckler et al., 1988; Armstrong, 1997; Moustafa, 2003; Woodman, 2009). The stratabound dolostone bodies are formed from the Oligocene to Early Miocene, when the base of the Thebes Fm. in the footwall of the HFF would be buried down to a depth of approximately -700 to -850 m. Movement on the Gebel Fault is thought to post-date the formation of the dolostone bodies based on cross-cutting relationships in the field. The black dashed line denotes the pre-rift/syn-rift boundary.

Figure 13. Conceptual fluid flow model which interprets that during the late Oligocene, seawater was drawn down incipient faults within the proto-footwall of the Hamman Faraun Fault and circulated by geothermal convection along the Nubian aquifer until they reached the proto-HFF. Fluids moved up the fault and were expelled laterally into the basal Thebes Formation where they migrated laterally.

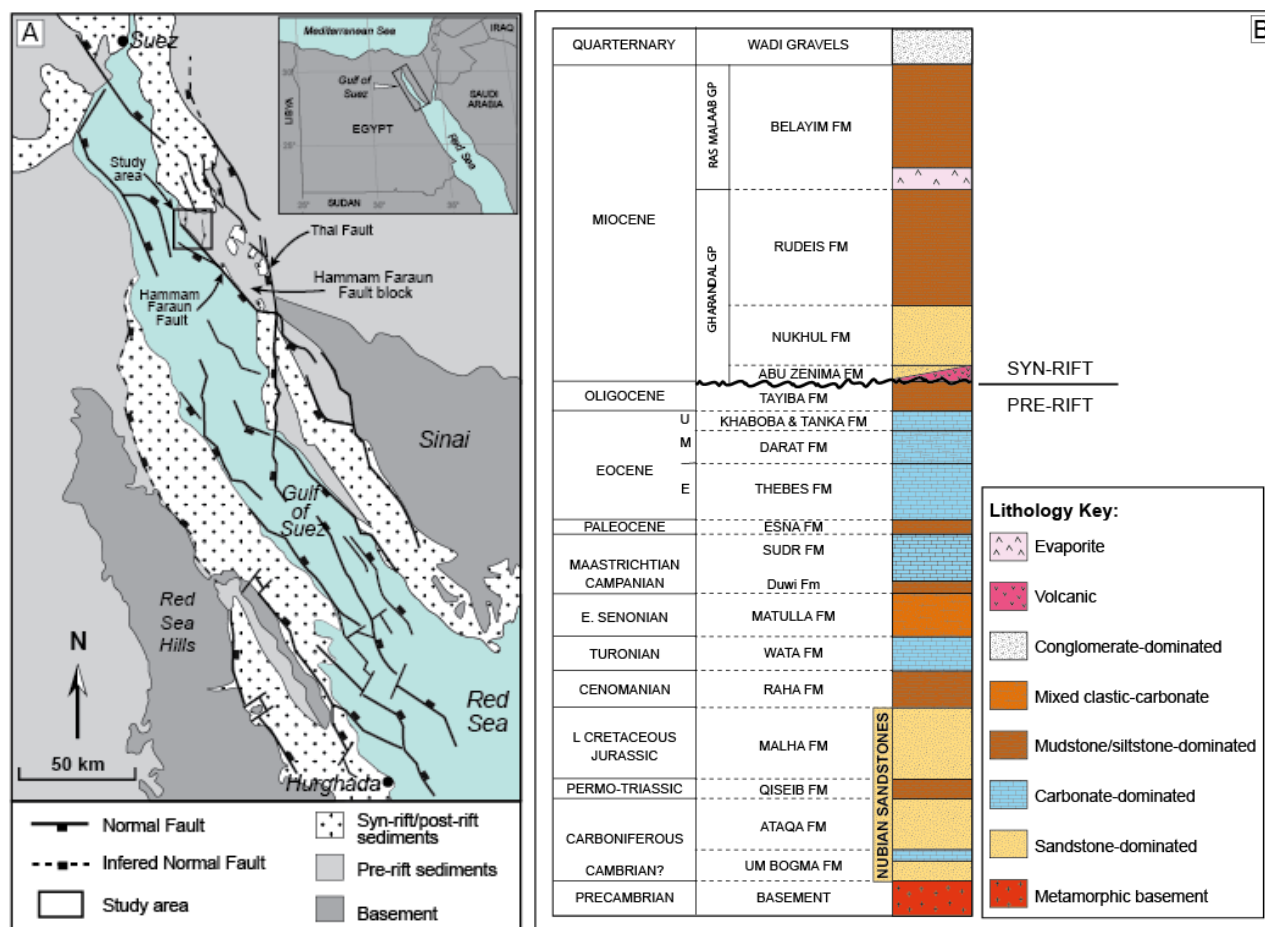


Fig. 1. (A) Map showing the major structural elements of the Gulf of Suez and distribution of pre-rift and syn-rift sediments along the western Sinai coast (adapted from Younes and McClay, 2002 and Khalil and McClay, 2002). **(B)** Composite stratigraphic section of the Hammam Faraun Fault block (adapted from Sharp *et al.*, 2000 and Jackson *et al.*, 2006). This study focuses on the pre-rift Thebes Formation.

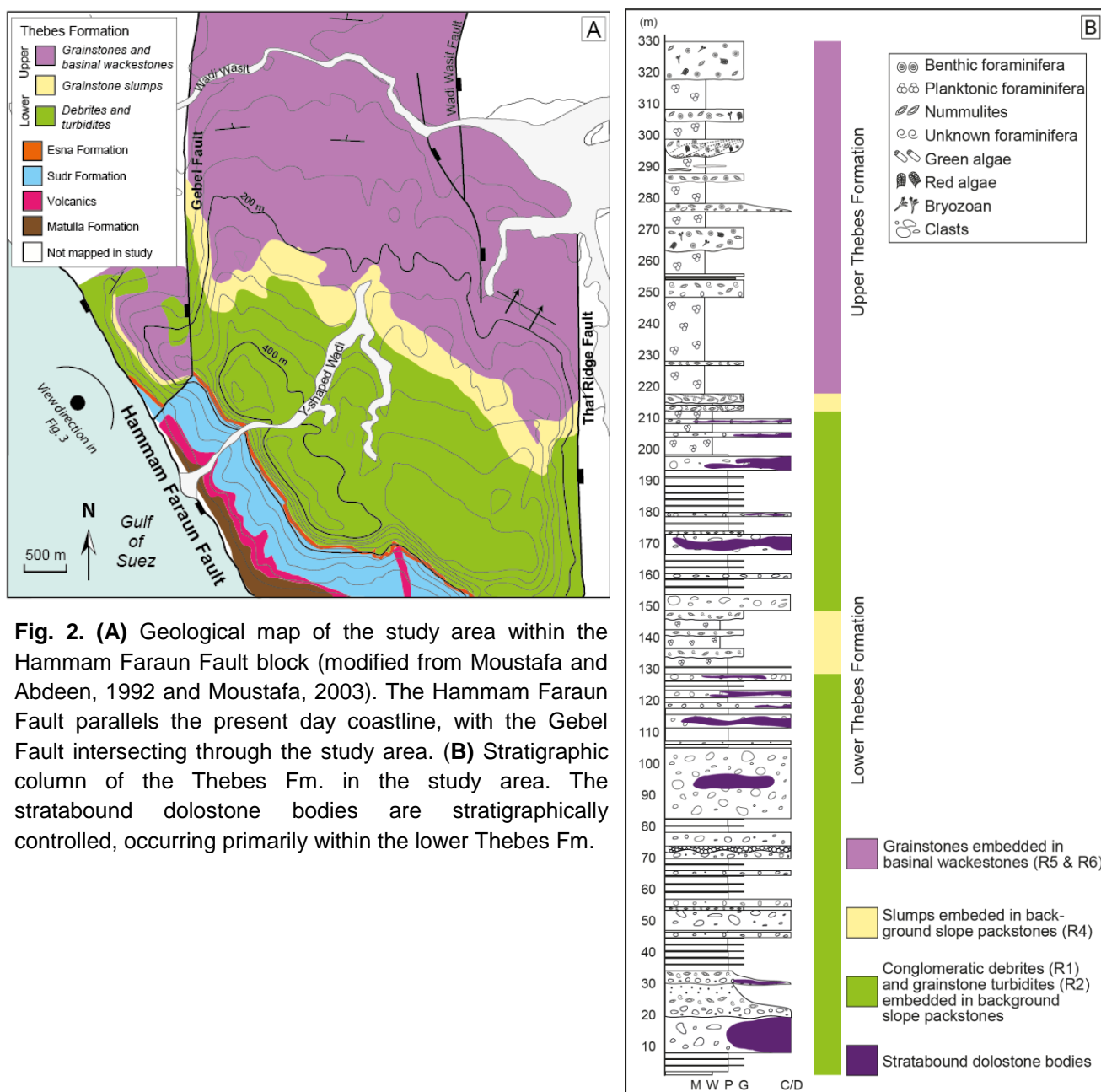


Fig. 2. (A) Geological map of the study area within the Hammam Faraun Fault block (modified from Moustafa and Abdeen, 1992 and Moustafa, 2003). The Hammam Faraun Fault parallels the present day coastline, with the Gebel Fault intersecting through the study area. **(B)** Stratigraphic column of the Thebes Fm. in the study area. The stratabound dolostone bodies are stratigraphically controlled, occurring primarily within the lower Thebes Fm.

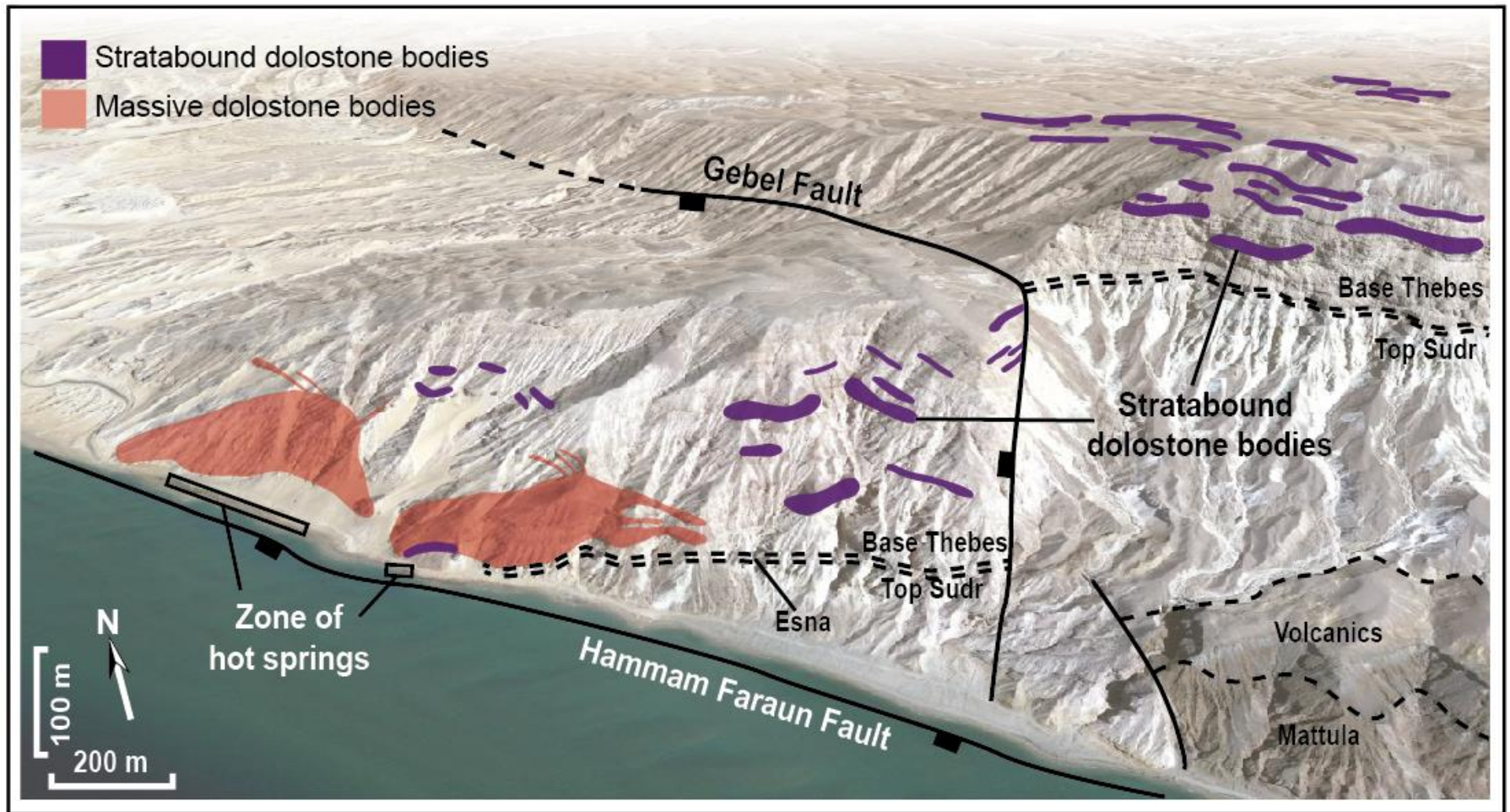


Fig. 3. Oblique view of study area (direction of view annotated in Fig. 2a) showing the distribution and extent of stratabound dolostone bodies relative to the Hammam Faraun Fault and the Gebel Fault, superimposed onto a Google Earth image. The origin of the massive dolostone bodies in the study area are further discussed in Hollis *et al.* (2017).

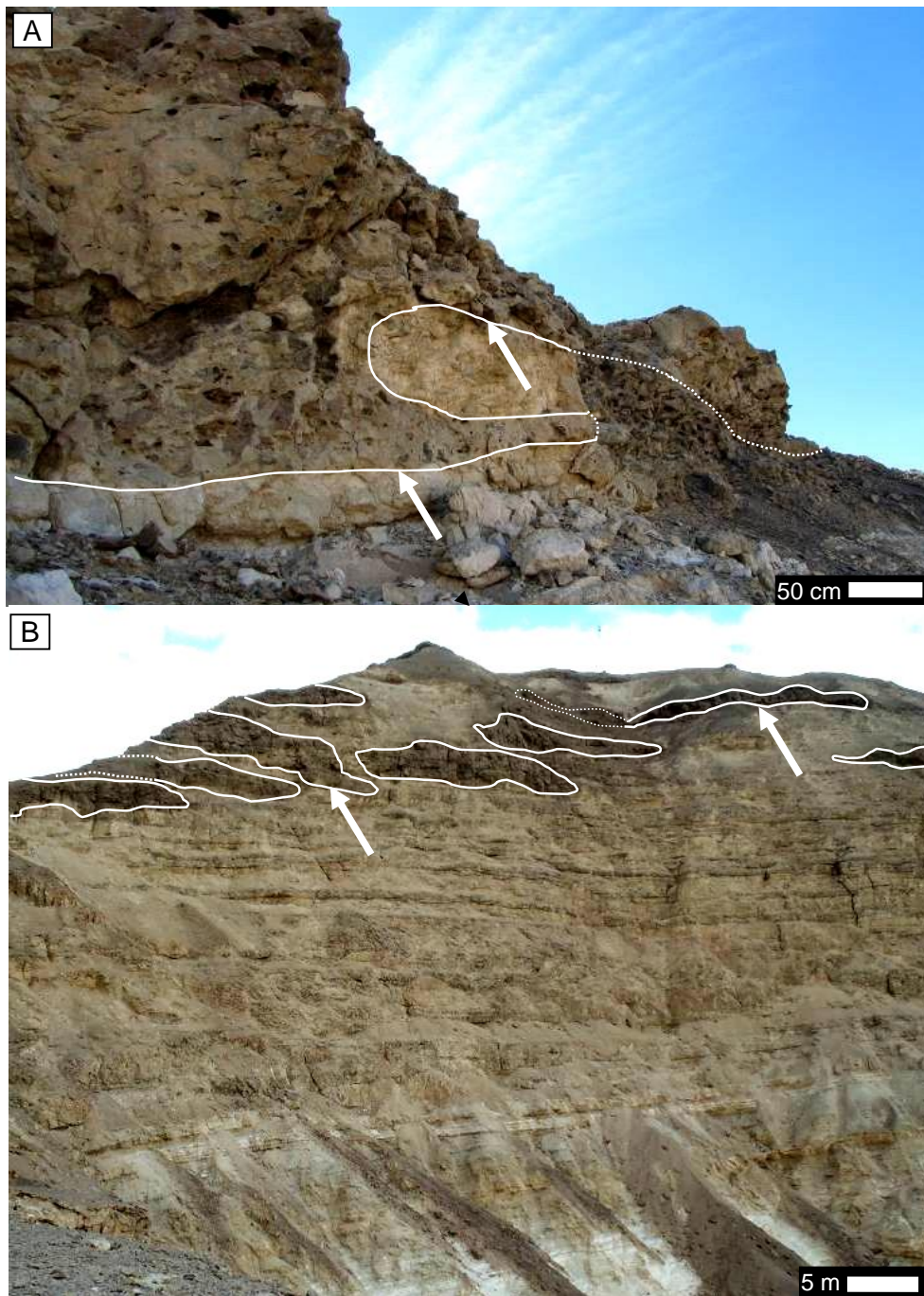


Fig. 4. (A) and (B) Sharp, planar contacts (arrows) between dark brown dolostone bodies and adjacent cream coloured host limestone beds.

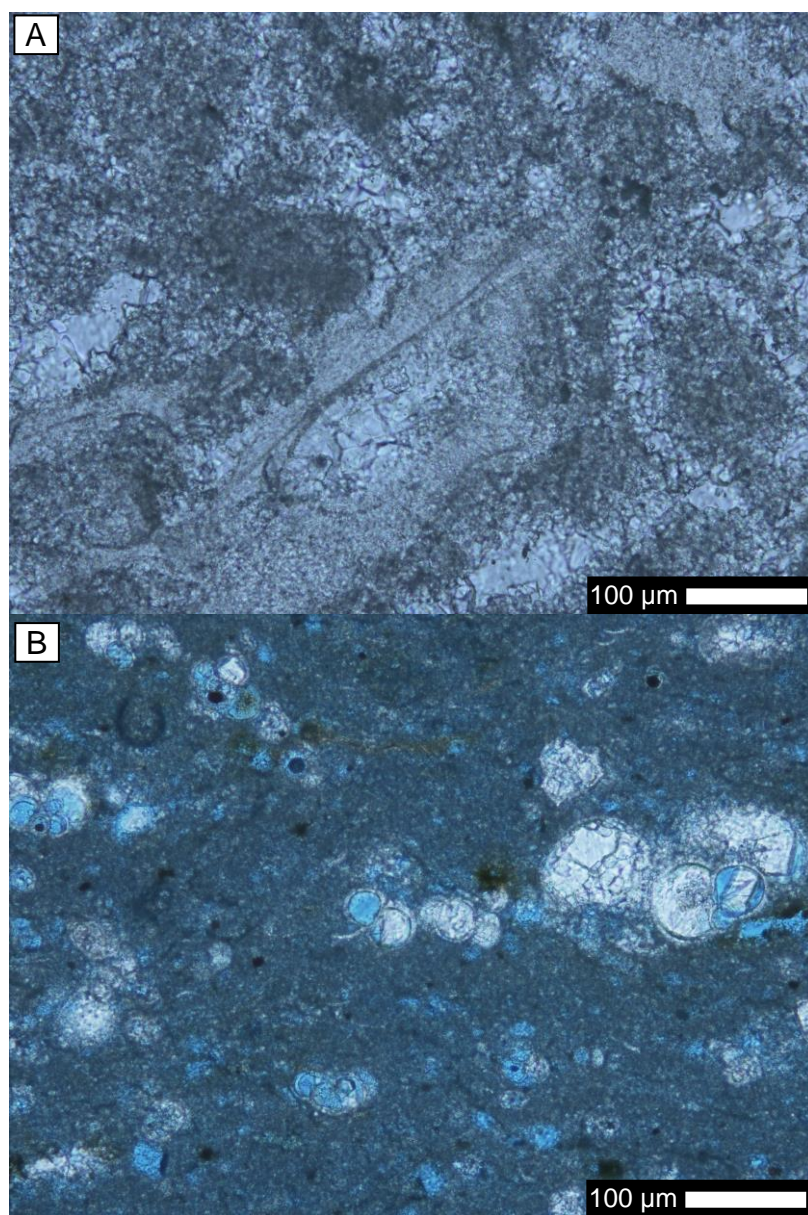
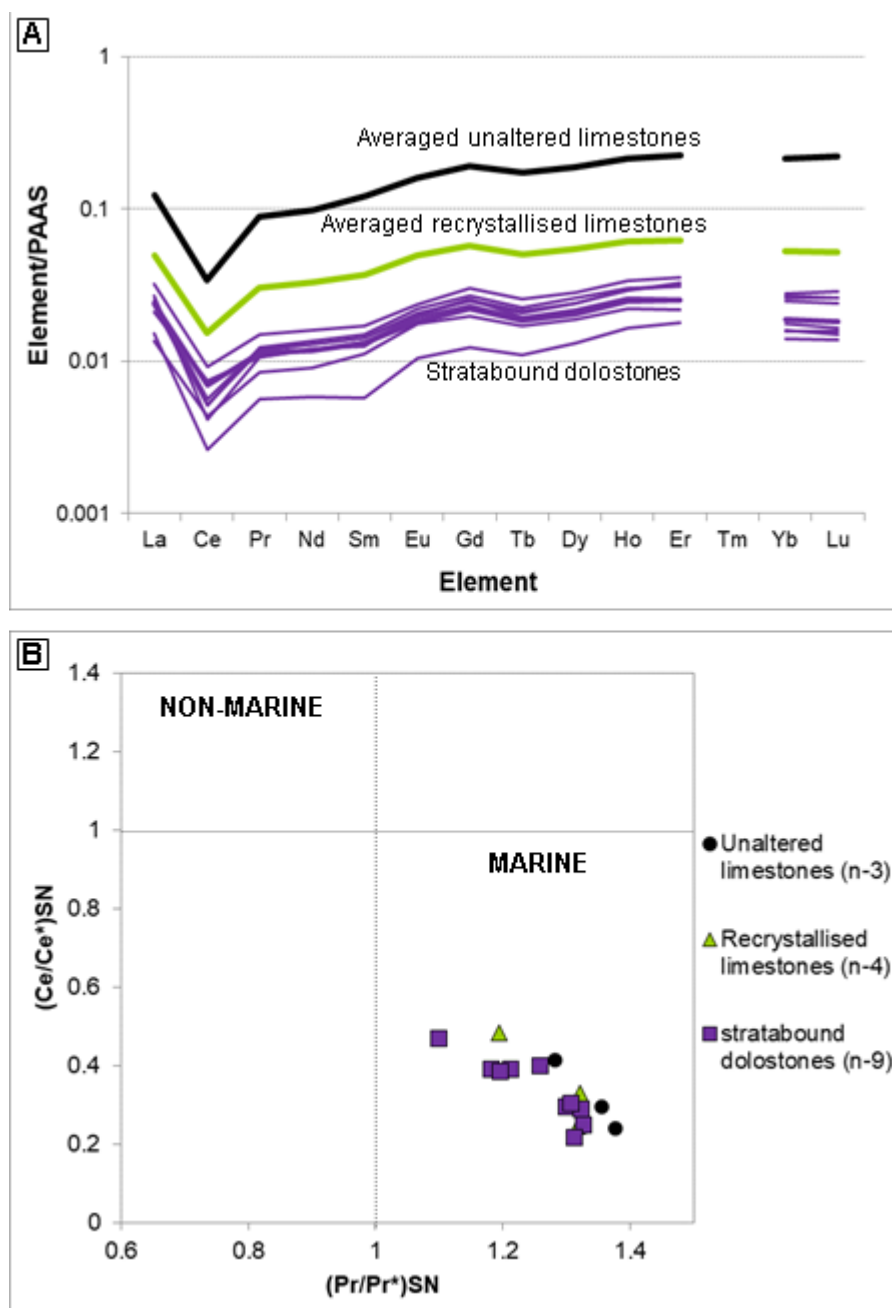


Figure 5. Photomicrographs showing the petrographic features of the precursor limestones in plane polarised light. **(A)** Recrystallised grainflow grainstone, with both matrix and allochems replaced by micro spar calcite. **(B)** Unaltered basinal wackestones, with microporous mud matrix and mosaic calcite within the internal structure of the pelagic foraminifera.



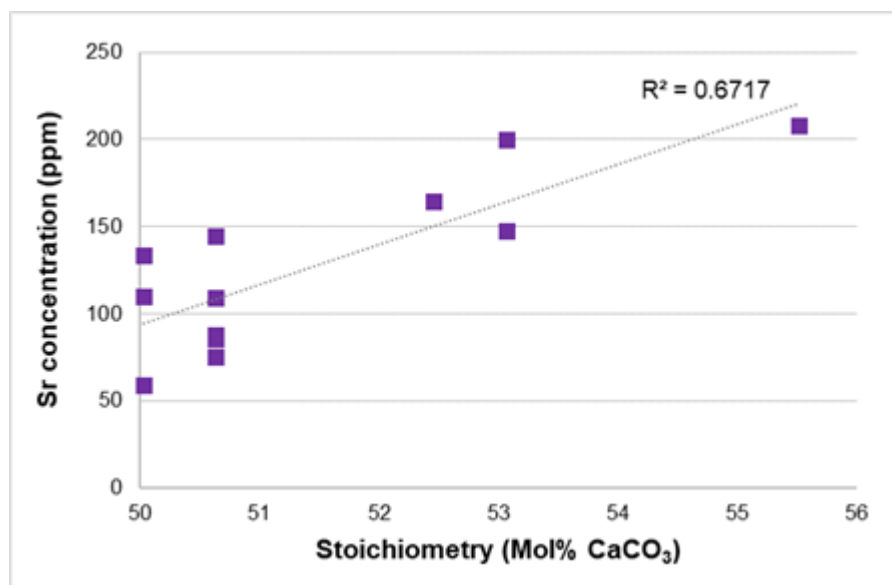
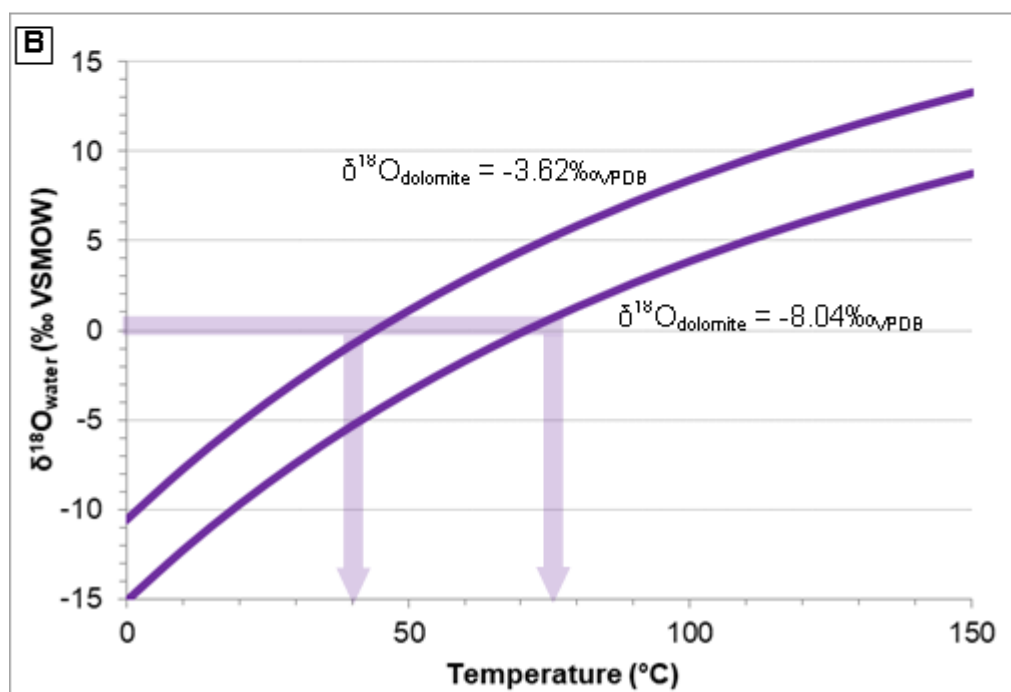
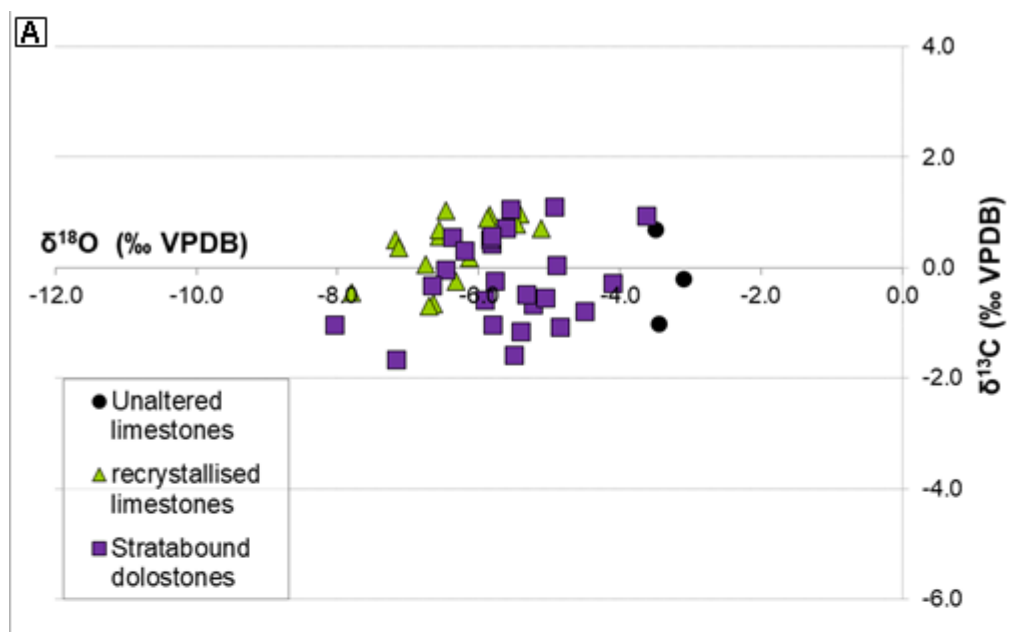


Fig. 6. (A) PAAS normalised REE concentrations comparing the REE patterns for averaged unaltered and recrystallised limestones to the stratabound dolostones. Positive La and negative Ce anomalies are present in each case, however a flattening in the HREE's is observed within the dolomite samples, as seen within the recrystallised limestone samples. A notable decrease in the total REE concentration of the stratabound dolomites is observed relative to the host limestones. **(B)** PAAS normalised $(Pr/Pr^*)_{SN}$ versus $(Ce/Ce^*)_{SN}$ cerium anomaly plot (Webb and Kamber, 2000) showing that all samples cluster tightly in the field of negative Ce and positive La anomalies. **(C)** Sr concentration relative to dolomite stoichiometry, illustrating an increase in Sr with increasing mol% CaCO₃, as per Vahrenkamp and Swart (1990), shown by dotted line.



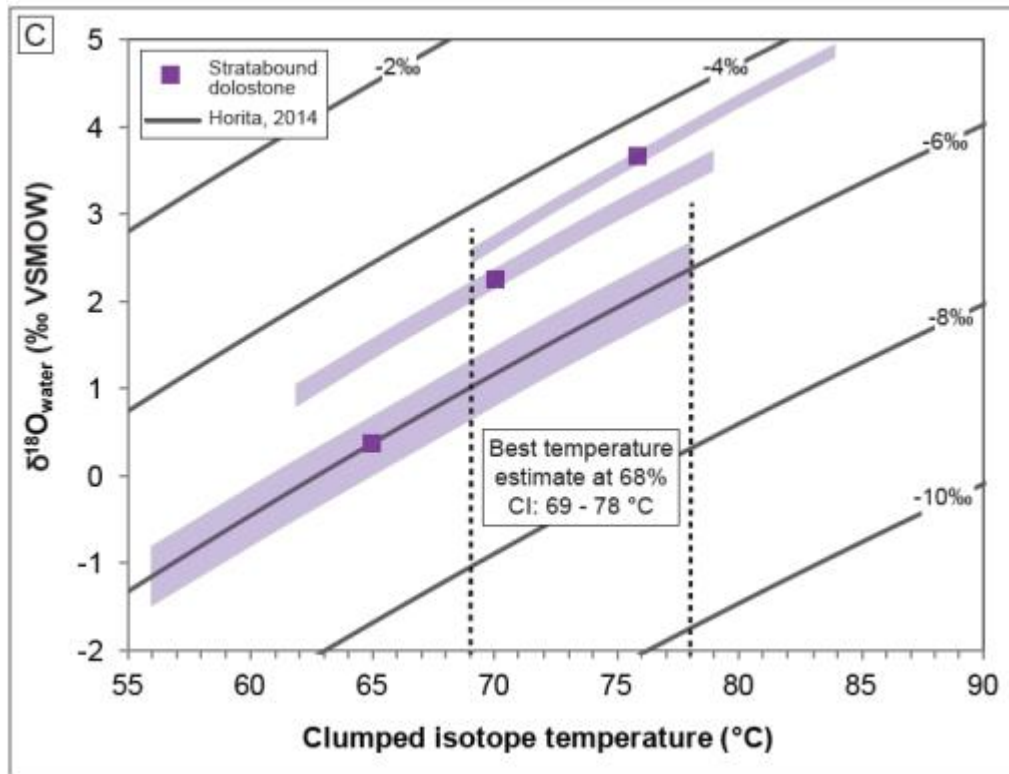


Fig. 7. (A) Stable isotope ($\delta^{18}\text{O}$ vs. $\delta^{13}\text{C}$) plot for unaltered limestones, recrystallised limestones, and stratabound dolostone samples. The whole rock isotopic composition for the unaltered limestones lie within the range that is expected for deposition from Eocene seawater (Pearson *et al.*, 2001). In comparison, the recrystallised limestone and dolostone samples exhibit lower $\delta^{18}\text{O}$ values ranging between $-3.62\text{‰}_{\text{VPDB}}$ and $-8.04\text{‰}_{\text{VPDB}}$. **(B)** Temperature of dolomitizing fluids versus $\delta^{18}\text{O}_{\text{seawater}}$ plot for the stratabound dolostone bodies. This plot is constructed using the Matthews and Katz (1977) fractionation equation and can be used to determine the minimum and maximum temperature of dolomitizing fluids using the heaviest and lightest $\delta^{18}\text{O}_{\text{dolomite}}$ values. Assuming a $\delta^{18}\text{O}_{\text{seawater}}$ of $+1\text{‰}$ to 0‰ (Veizer and Prokoph, 2015), a minimum fluid temperature of 40°C and a maximum fluid temperature of 78°C would be expected. **(C)** Clumped isotope temperatures (y-axis, $^\circ\text{C}$) versus calculated $\delta^{18}\text{O}_{\text{water}}$ (x-axis, ‰ VSMOW) for three dolomite samples in this study. The shaded area represents the 68% confidence interval for each sample. Dashed lines represent the temperature range at which all three samples overlap at the 68% confidence interval ($69\text{--}78^\circ\text{C}$); this corresponds to a calculated fluid composition of approximately 2.5‰ VSMOW .

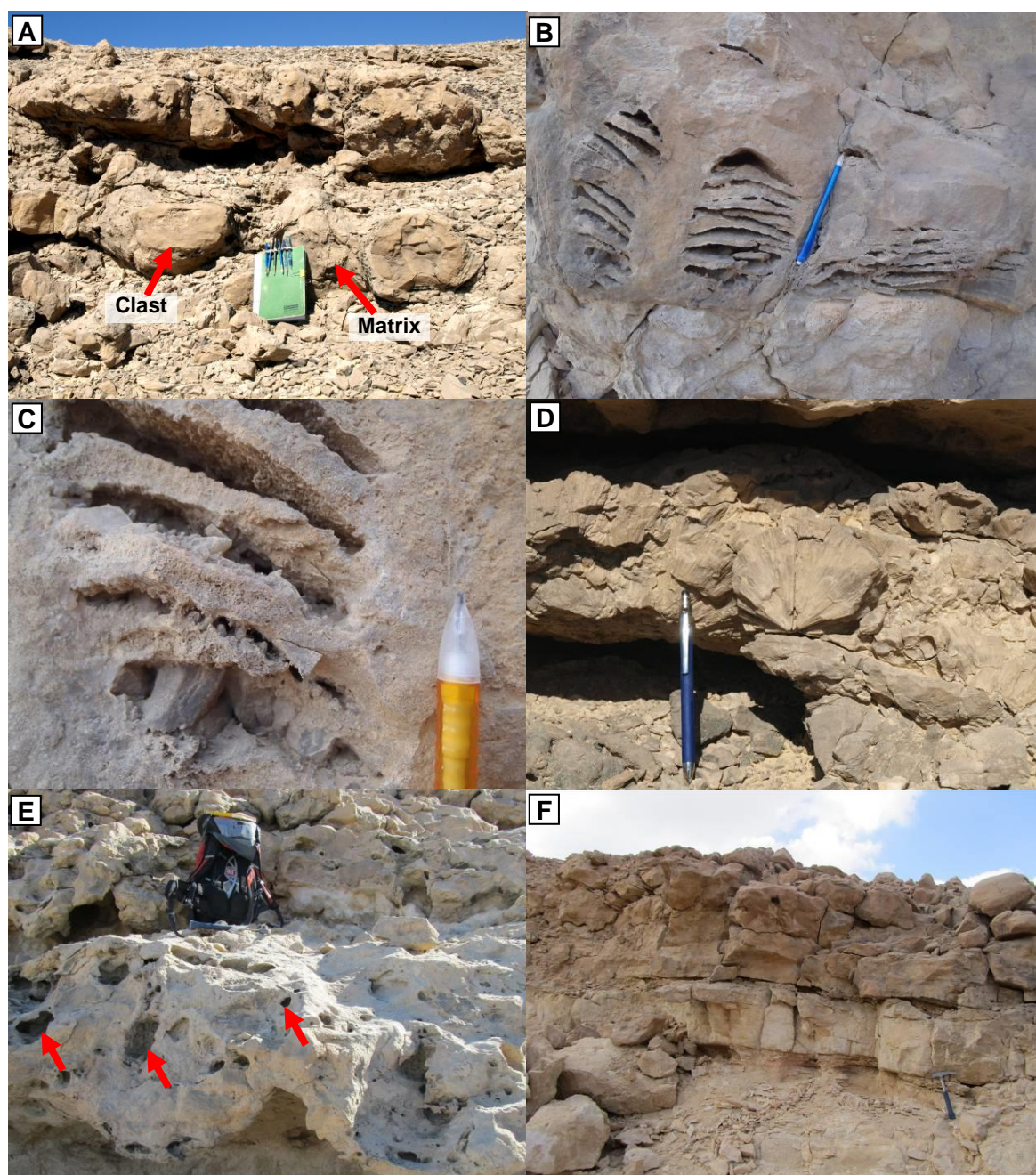


Fig. 8. Macroscopic features of the stratabound dolostone bodies in the field. **(A)** Dark brown clast and grey matrix fabric within the stratabound bodies, both composed of dolomite. **(B)** Randomly orientated zebra dolomite-like fabrics, with elongated vuggy porosity. **(C)** Dogtooth calcite cement partially occluding vuggy porosity within zebra fabric. **(D)** Large botryoidal calcite cement partially cementing vuggy porosity. **(E)** Mouldic pores after clasts (arrow) of variable size. **(F)** Stratabound dolostone body lacking the presence of clast, clast pores or large vuggy pores, indicating dolomitisation of grainstone turbidite (R2) facies.

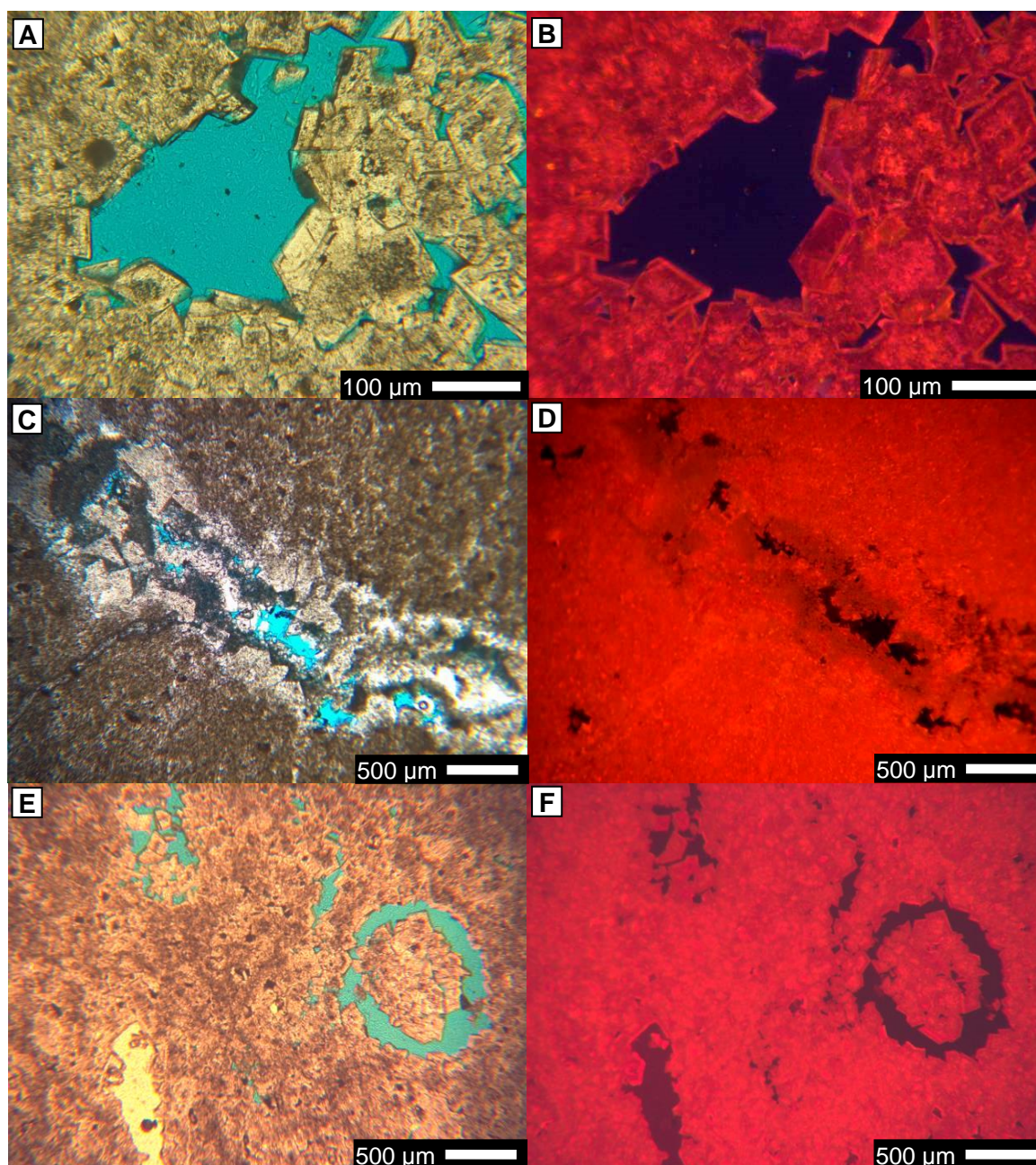


Fig. 9. Photomicrographs of various dolomite textures, in plane polarised light (PPL, left) and cathodoluminescence (CL, right). **(A)** Planar-s dolomite in PPL and **(B)** in CL, showing mottled bright red and orange luminescent dolomite cores, overlain by a thick dull green luminescent zone and a thin bright red luminescent outer zone. **(C)** Matrix with non-planar dolomite texture in PPL, **(D)** corresponding CL image of non-planar dolomite showing mottled bright red and orange luminescence with limited zonation. **(E)** Non-planar dolomite in PPL and **(F)** corresponding CL image with mottled red and orange luminescence with zonation difficult to identify.

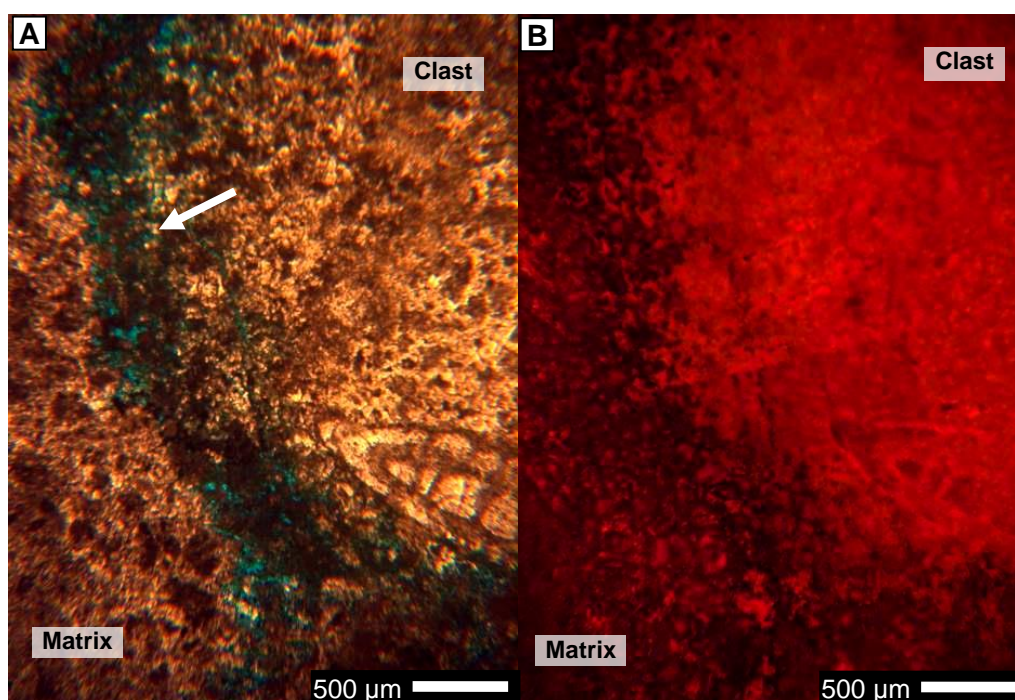


Fig. 10. (A) Photomicrograph in PPL of cloudy core clear rim planar-s dolomite texture within a clast, and non-planar dedolomitised matrix. The clast and matrix are separated by a corrosion rim (arrow), **(B)** corresponding CL image with clast exhibiting mottled bright red and orange luminescent dolomite crystals. The matrix primarily exhibits non-luminescence, with minor patches of bright red and orange luminescence.

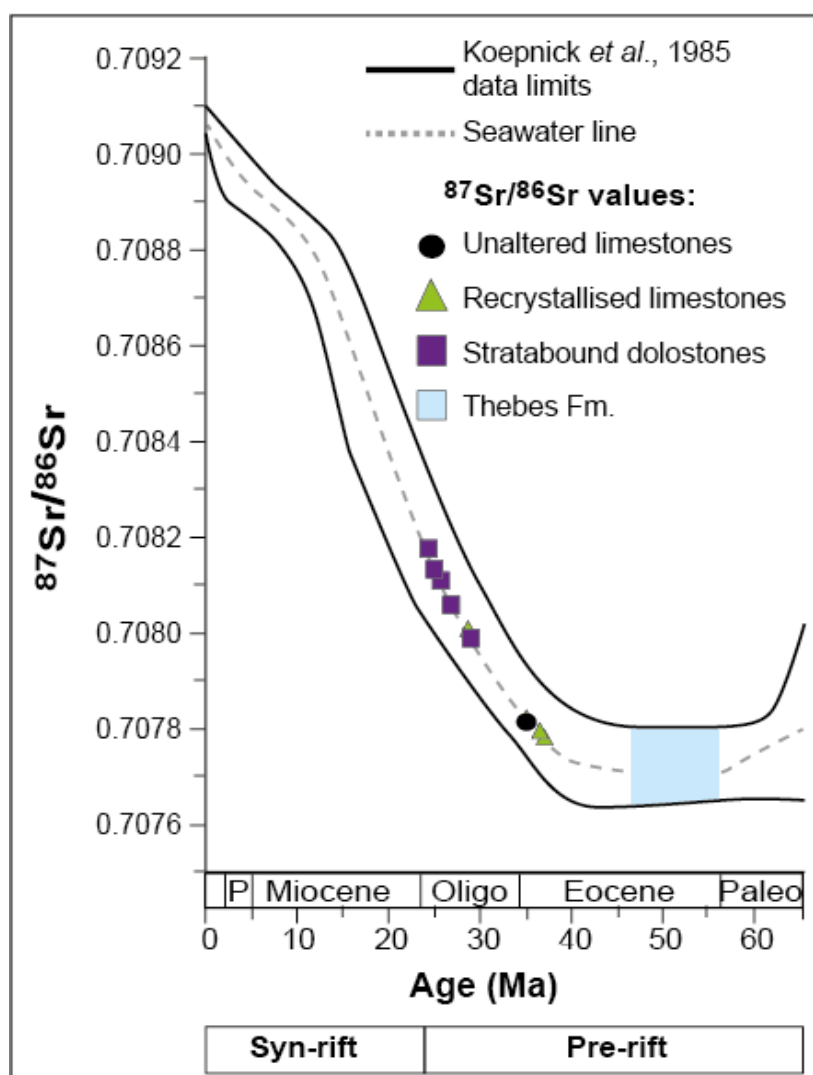


Fig. 11. Strontium isotopic ratios relative to the seawater strontium curve (Koeppnick *et al.*, 1985) and tectonic events of the Hammam Faraun Fault block. The time of formation of the Thebes Fm. is also highlighted. The unaltered and recrystallised limestones correspond to Late Eocene to Early Oligocene seawater. The stratabound dolostone bodies correspond to middle Oligocene to Early Miocene seawater strontium ratios, and the late pre-rift to rift initiation tectonic phase.

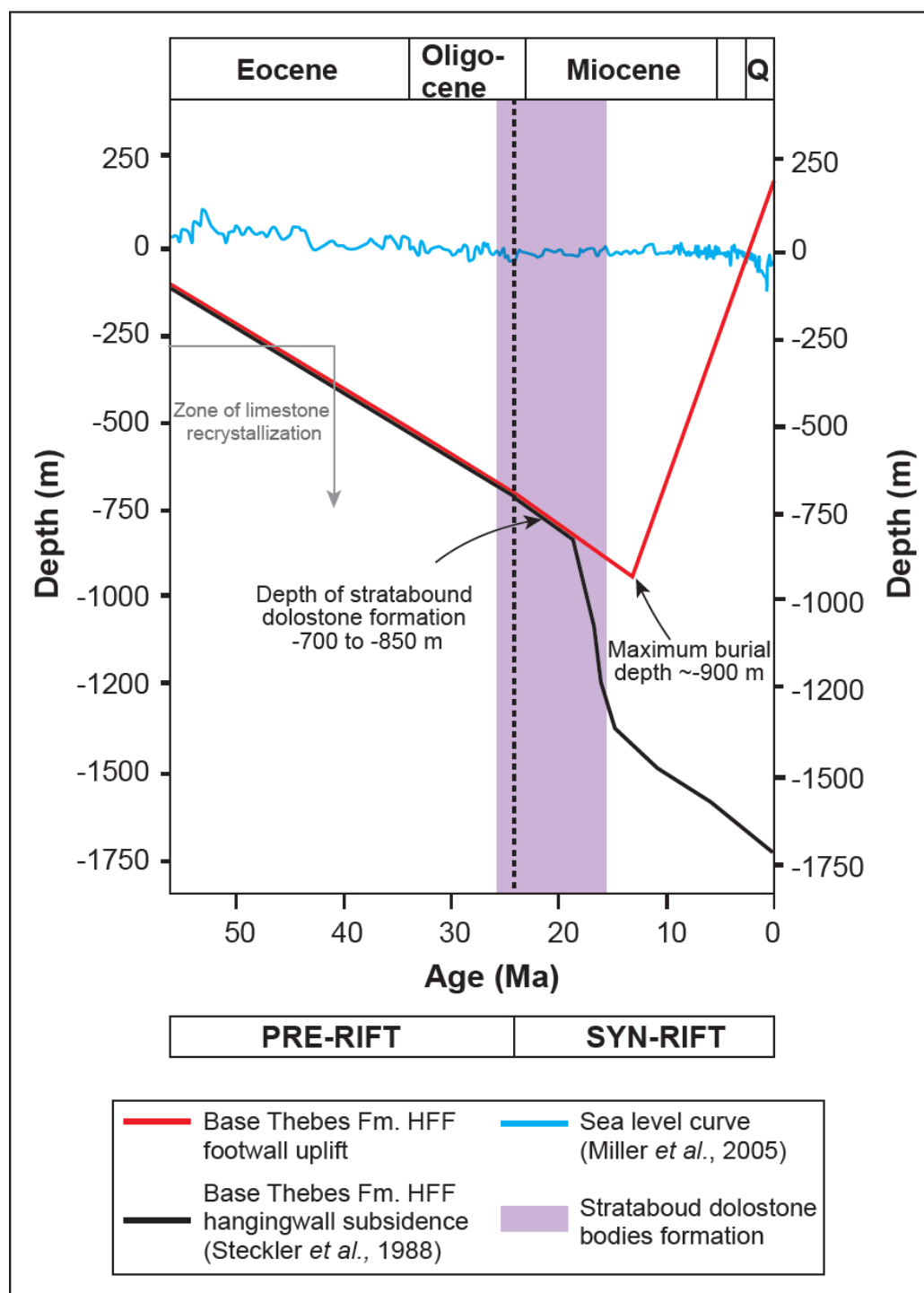


Fig. 12. Burial history curve for the base Thebes Fm. in the hangingwall and footwall of the Hammam Faraun Fault block. Knowledge of the pre-rift and syn-rift sediment deposition is utilised to construct the burial history for both the hangingwall and footwall succession (Steckler *et al.*, 1988; Armstrong, 1997; Moustafa, 2003; Woodman, 2009). The stratabound dolostone bodies are formed from the Oligocene to Early Miocene, when the base of the Thebes Fm. in the footwall of the HFF would be buried down to a depth of approximately -700 to -850 m. Movement on the Gebel Fault is thought to post-date the formation of the dolostone bodies based on cross-cutting relationships in the field. The black dashed line denotes the pre-rift/syn-rift boundary.

F

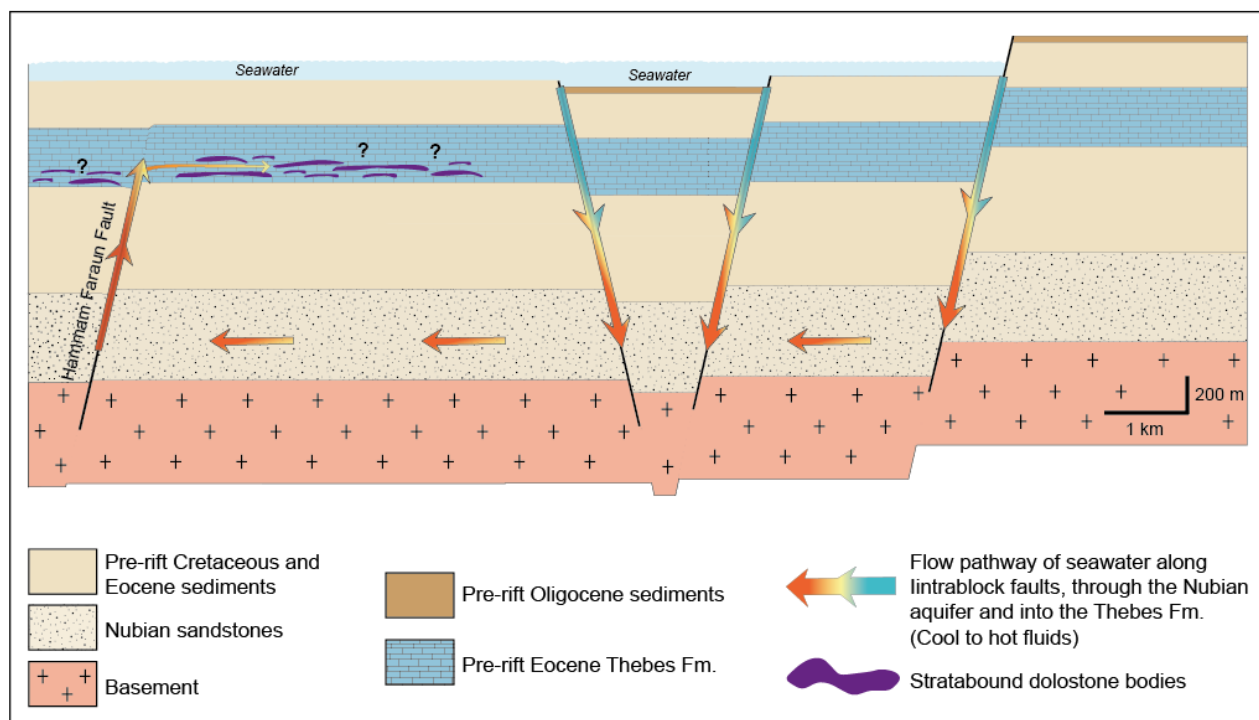


Fig. 13. Conceptual fluid flow model which interprets that during the late Oligocene, seawater was drawn down incipient faults within the proto-footwall of the Hamman Faraun Fault and circulated by geothermal convection along the Nubian aquifer until they reached the proto-HFF. Fluids moved up the fault and were expelled laterally into the basal Thebes Formation where they migrated laterally.

Deposit type	Facies type	Facies Code	Basal contact	Upper contact	Depositional texture	Allochems	Helium porosity (%)	Kh (mD)	Pore type	Notes
In-situ deposit	Basinal wackestones	B1	Regular	Irregular or scoured	Wackestone	planktonic foraminifera, small <i>Nummulites</i> , uni- and bi-serial foraminifera, echinoid fragments	24% (9-39%, n=7)	1.07 mD (0.04-3.5, n=7)	Microporosity in matrix	Sedimentary laminations may be visible with layered foraminifera
In-situ deposit	Slope packstones	S1	Regular	Irregular or scoured	Packstone, intercalated with thin grainstone beds	<i>Nummulites</i> , <i>Dyscocyclina</i> , <i>Alveolinids</i> , <i>Operculina</i> , planktonic foraminifera, echinoid fragments, bryozoan fragments	13% (9-35%, n=8)	0.30 mD (<0.01 - 1.7, n=8)	Microporosity in matrix, intragranular	Commonly recrystallised skeletal material and mud matrix.
Remobilised deposit	Matrix-supported conglomerate in slope deposits	R1	Irregular	Rounded	Matrix - foraminifera wackestone Clast - Skeletal packstone and grainstone	Matrix - mixed <i>Nummulites</i> , <i>Alveolinids</i> , planktonic foraminifera, echinoid fragments. Some clasts Clasts - <i>Nummulites</i> , <i>Operculina</i> , <i>Alveolinids</i> , bryozoa fragments, echinoid fragments	9% (<1-17%, n=8) Dolomite = 4% (1-7%)	0.35 mD (<0.01 - 1.5, n=8) Dolomite = 0.12mD (<0.01 – 0.6 mD)	Matrix - microporosity Clasts - low to none	Subangular to subrounded clasts. Some clasts are composed of neomorphic calcite cement, fabric destructive and/or retentive. Some clasts are dolomitised.
Remobilised deposit	Foraminifera grainstone turbidite in slope deposits	R2	Irregular	sharp	Foraminiferal grainstone	<i>Nummulites</i> , <i>Alveolinids</i> , <i>Miliolids</i> , <i>Operculina</i> , serpulid worm	16.5% (16-17%, n=2)	1.5mD (0.8 – 2.2, n=2)	intergranular	Little to no matrix. Intergranular porosity is commonly plugged by calcite cement. Evidence of fining upward cycles

						tubes, echinoid fragments, red algal fragments, bryozoan fragments	Dolomite = 2% (1-3%)	Dolomite = 0.2mD (<0.01 – 0.56mD)		
Remobilised deposit	Clast-supported debris sheet flow in slope deposits	R3	scoured	sharp	Matrix - wackestone Clasts - Algal foraminifera grainstone	Matrix – small Nummulites Clasts - <i>Miliolids</i> , <i>Soritids</i> , <i>Nummulites</i> , <i>Alveolinids</i> , dasyclad algae, red algae, algal filaments, bryozoan fragments .	nd	nd	Matrix - high microporosity Clasts - Minor mouldic and intercrystalline	Rounded to subrounded clasts. possibly debris sheet flow
Remobilised deposit	Slump grainstones in slope deposits	R4	scoured	regular	Packstone and grainstone	dasyclads, <i>Nummulites</i> , <i>Operculina</i> , <i>miliolids</i> , <i>echinoid fragments</i> , <i>green algae</i>	nd	nd	little to none	Convolute bedding. Porosity often cemented by calcite. Contains little to no mud matrix
Remobilised deposit	Grainstones in basinal deposits	R5	Irregular	sharp	Grainstone	<i>Nummulites</i> , <i>Alveolinids</i> , <i>Miliolids</i> , <i>Operculina</i> , echinoid fragments, red algal fragments, bryozoan fragments	10% (1 - 20%, n=16)	0.28mD (0.01 – 1.4, n=2)	mouldic and intergranular	Little to no matrix. Geobodies often mimetically silicified
Remobilised deposit	Channel grainstones in basinal deposits	R6	scoured	sharp	Grainstone	dasyclad algae, <i>Nummulites</i> , <i>Miliolids</i> , <i>Alveolinids</i> , <i>Soritids</i> , red algae, bryozoans fragments, serpulid worm tubes, echinoid fragments, mollusc fragments	18% (3 - 10%, n=3)	0.3mD (0.01 – 0.8, n=3)	minor intercrystalline	Lateral accretionary surfaces visible in cross-section. Channels bypass grainflow deposits, no evidence of cross-cutting relationships

Table 1. Facies descriptions for the Thebes Formation in the study area (after Corlett *et al.*, in prep). The Lower Thebes Formation is composed primarily of facies S1, R1, R2, R3 and R4, and the Upper Thebes Formation is made up of facies B1, R5 and R6.

Phase	mole% CaCO ₃	Mg (ppm)	Ca (ppm)	Fe (ppm)	Mn (ppm)	Al (ppm)	Sr (ppm)	Ni (ppm)	Ba (ppm)	d ¹³ C VPDB	d ¹⁸ O VPDB	d ¹⁸ O VSMOW	⁸⁷ Sr/ ⁸⁶ Sr
-------	----------------------------	-------------	-------------	-------------	-------------	-------------	-------------	-------------	-------------	---------------------------	---------------------------	----------------------------	------------------------------------

Unaltered limestones

n	-	3	3	3	3	3	3	3	3	3	3	3	1
min	-	2127	304691	1753	14.5	1928	933	29.5	8.0	-1.00	-3.50	27.30	-
mean	-	6327	313390	2182	16.9	2150	1240	40.3	20.7	-0.17	-3.35	27.45	0.707814
max	-	12362	320615	2648	21.5	2305	1775	48.8	32.5	0.70	-3.10	27.70	-
st dev	-	5359	8064	449	4.0	197	465	9.8	12.3	0.85	0.22	0.22	-

Recrystallised limestones

n	-	3	3	3	3	3	3	3	3	16	16	16	4
min	-	2523	349901	97	43	134	415	2.6	4.6	-0.69	-7.80	22.87	0.707773
mean	-	5108	358407	145	138	220	576	6.6	11.7	0.35	-6.37	24.32	0.707849
max	-	6534	367722	217	273	372	664	12.9	17.8	1.04	-5.12	25.65	0.708011
st dev	-	2243	8938	64	120	132	140	5.5	6.6	-0.59	-0.71	-0.77	-0.000109

Stratabound dolostones

n	16	18	10	18	18	18	18	18	18	24	24	24	5
min	50.03	32287	99518	37	208	23	59	0.6	8	-1.67	-8.04	22.62	0.707992
mean	51.34	75785	213098	151	463	107	142	5.2	137	-0.27	-5.70	25.04	0.708123
max	55.52	92590	313765	411	991	191	232	25.0	590	1.09	-4.10	26.70	0.708241
st dev	1.54	18255	53348	112	237	60	48	6.1	162	0.80	0.86	0.89	9.79E-05

Table 2. Summary of geochemical data collected from unaltered limestones, recrystallised limestones and stratabound dolostones. Dolomite stoichiometry is determined using Lumsden's equation (1979). Trace element concentrations are measured using ICP-MS and ICP-AES. Stable isotopic concentrations are determined using a carbonate CO₂ extraction line, and the resulting gas is analysed by mass spectrometry. Strontium isotopic ratios are measured with a Triton Thermal Ionization Mass Spectrometer.

a	Stoichiometry (mole% CaCO ₃)	$\delta^{18}\text{O}_{\text{carbonate}}$ (VPDB) ^a	$\delta^{13}\text{C}$ (VPDB) ^a	Δ_{47} ^b	T (°C) ^b	$\delta^{18}\text{O}_{\text{water}}$ (SMOW)
Sample						
11B	50.6	- 4.59 (0.03)	- 0.72 (0.02)	0.561 ± 0.004	76 ± 8	3.6±1.0‰
34C	50.0	- 6.01 (0.36)	0.49 (0.02)	0.580 ± 0.008	67± 11	0.6±1.0‰
81A	53.1	- 4.86 (0.06)	1.06 (0.05)	0.575 ± 0.008	70 ± 9	2.3±1.3‰

b	Temperature at +0.6‰ SMOW	Temperature at +3.6‰ SMOW	Fluid at 67°C	Fluid at 76°C
Minimum $\delta^{18}\text{O}_{\text{dol}} = -8.0\text{‰ PDB}$	61°C	83°C	+1.5‰	+2.7‰
Mean $\delta^{18}\text{O}_{\text{dol}} = -5.5\text{‰ PDB}$	45°C	64°C	+4.1‰	+5.3‰
Max $\delta^{18}\text{O}_{\text{dol}} = -4.0\text{‰ PDB}$	36°C	54°C	+5.6‰	+6.9‰

Table 3 (a) Summary of isotopic composition, Δ_{47} , temperature and $\delta^{18}\text{O}_{\text{fluid}}$ for stratabound dolostones as determined from clumped isotope analysis. a= Error is 1 σ for $\delta^{13}\text{C}$ and $\delta^{18}\text{O}$ carbonate, b= Error for Δ_{47} and temperature (T) is given as standard error, calculated by the replicate standard deviation divided by square root of n. Dolomite stoichiometry determined as per Lumsden (1979), **(b)** Range of possible fluid temperatures and $\delta^{18}\text{O}$ water using clumped isotope constraints based on conventional isotope data, based on Matthews and Katz (1977).

Assuming 25°C and 70% humidity

$\delta^{18}\text{O}_{\text{water}}$	1.03
T	25°C
h	0.70
f	0.3
$\delta\alpha$	-2
δo	0.6
A	-1.83
B	-3.10

$\delta^{18}\text{O}_{\text{water}}$	1.19
T	25°C
h	0.70
f	0.4
$\delta\alpha$	-2
δo	0.6
A	-1.67
B	-2.98

$\delta^{18}\text{O}_{\text{water}}$	0.98
T	25°C
h	0.70
f	0.5
$\delta\alpha$	-2
δo	0.6
A	-1.59
B	-2.92

Assuming 30°C and 50% humidity

$\delta^{18}\text{O}_{\text{water}}$	5.52
T	30°C
h	0.5
f	0.3
$\delta\alpha$	-2
δo	0.6
A	-0.48
B	-2.19

$\delta^{18}\text{O}_{\text{water}}$	3.05
T	30°C
h	0.5
f	0.4
$\delta\alpha$	-2
δo	0.6
A	-0.45
B	-2.16

$\delta^{18}\text{O}_{\text{water}}$	1.97
T	30°C
h	0.5
f	0.5
$\delta\alpha$	-2
δo	0.6
A	-0.43
B	-2.15

$\delta^{18}\text{O}_{\text{water}}$	$\delta^{18}\text{O}$ of residual water body= $(\delta\text{o}-A/B)f^B+A/B$
δo	$\delta^{18}\text{O}$ composition of original water
δa	$\delta^{18}\text{O}$ of atmospheric moisture
α	equilibrium fractionation between O and H ₂ O, based on Kakiuchi and Matsuo, 1979
αw	activity coefficient of water= $-0.000543f^{-2} - 0.018521f^{-1} + 0.99931$
h	humidity
τ	ratio of activity coefficients for $^{18}\text{O}/^{16}\text{O}$ where $(t^{-1} - 1) \times 10^3 = 0.47\text{mCaCl}_2 + 1.107\text{mMgCl}_2 - 0.16\text{mKCl}$
$\Delta\epsilon$	kinetic enrichment factor, $\Delta\epsilon=k((1-h)/\alpha\text{w})$
ϵ	$\alpha - 1$
f	fraction of water evaporated
A =	$((h/\alpha\text{w}) * \delta\text{a} + \Delta\epsilon + (\alpha-t))/\alpha / 1 - (h/\alpha\text{w}) + \Delta\epsilon$
B =	$(h/\alpha\text{w}) - \Delta\epsilon + (\alpha-t))/\alpha / (1-h)/(\alpha\text{w} + \Delta\epsilon)$

Calculation assumes molality $\text{CaCl}_2 = 0.4$, $\text{MgCl}_2 = 1.48$ and $\text{KCl} = 0.28$

Table 4. Calculation of the $\delta^{18}\text{O}_{\text{water}}$ of the dolomitizing fluid, based on Swart *et al.*, 1989.

Temperature (°C)	65	65	65	80	80	80
Concentration Factor (x times seawater)	1	1.43	2	1	1.43	2
Density of dolomite (g/m ³)	2840000	2840000	2840000	2840000	2840000	2840000
Molecular weight of dolomite (g/mole)	184.4	184.4	184.4	184.4	184.4	184.4
Moles dolomite per m ³ at 0% porosity (mole/m ³)	15401	15401	15401	15401	15401	15401
Moles dolomite per m ³ at 19% porosity (mole/m ³)	12475	12475	12475	12475	12475	12475
Moles dolomite precipitated per kg water (mole)	0.01	0.02	0.03	0.01	0.01	0.02
kg water to precipitate 1 mole dolomite (kg)	77.06	53.97	38.13	100.87	70.52	50.25
Density of fluid (kg/m ³)	1005	1015	1027	996	1006	1019
m ³ fluid to ppt 1 mole dolomite (m ³)	0.077	0.053	0.037	0.101	0.070	0.049
^a Volume of fluid to precipitate 1m ³ dolomite (m ³)	957	664	463	1264	875	615
Distance from HFF (m)	2,000	2,000	2,000	2,000	2,000	2,000
^b Thickness of Thebes (m)	200	200	200	200	200	200
Width of block containing SBD (m)	1	1	1	1	1	1
Total volume of 1m slice in which SBD is observed (m ³)	400,000	400,000	400,000	400,000	400,000	400,000
^c Volume of SBD in 1 m slice (assume 19% dolomitized) (m ³)	76,000	76,000	76,000	76,000	76,000	76,000
^d Total volume of fluid (m ³) required to dolomitise 1m wide slice of SBD with 19% porosity (^c) (hanging wall only) at the given dolomitization potential (^a) determined by the fluid temperature and concentration factor	72,725,808	50,432,610	35,182,467	96,030,421	66,477,165	46,770,682

Total volume of fluid (m ³) required to dolomitise 1m wide slice of SBD with 19% porosity (²) (hanging wall and footwall) at the given dolomitization potential (¹) determined by the fluid temperature and concentration factor	145,451,616	100,865,219	70,364,933		192,060,841	132,954,330	93,541,365
^e Time available to dolomitise (year)	10,000,000	10,000,000	10,000,000		10,000,000	10,000,000	10,000,000
^f Total fluid flux required into footwall (m ³ /year)	7.27	5.04	3.52		9.60	6.65	4.68
^g Fluid flux per m ² of footwall	1.01	0.70	0.49		1.33	0.92	0.65
Pore velocity in SBD within footwall assuming all porosity is effective (m/year)	38.3	26.5	18.5		50.5	35.0	24.6
Pore velocity in SBD within footwall and hanging wall assuming all porosity is effective (m/year)	76.6	53.1	37.0		101.1	70.0	49.2
Horizontal velocity if 19% of vertical thickness is dolomite and 200 m vertical thickness m/yr	1.01	0.70	0.49		1.33	0.92	0.65

Table 5 Mass balance and velocity of dolomitizing fluids at 65°C and 80°C